AGU PUBLICATIONS

JGR

Journal of Geophysical Research: Solid Earth

RESEARCH ARTICLE

10.1002/2014JB011639

**Key Points:**
- Bayesian surface reconstruction scheme for sea level variation in twentieth century
- Dynamic Voronoi models adapted to strong spatial heterogeneity of tide gauge
- Probabilistic solution accounts for variable resolution among six large regions

**Correspondence to:**
G. Choblet,
gael.choblet@univ-nantes.fr

**Citation:**
Choblet, G., L. Husson, and T. Bodin (2014), Probabilistic surface reconstruction of coastal sea level rise during the twentieth century, *J. Geophys. Res. Solid Earth*, *119*, 9206–9236, doi:10.1002/2014JB011639.

Received 26 SEP 2014
Accepted 4 NOV 2014
Accepted article online 17 NOV 2014
Published online 19 DEC 2014

# Probabilistic surface reconstruction of coastal sea level rise during the twentieth century

**Gaël Choblet[1], Laurent Husson[2,3], and Thomas Bodin[4]**

[1]Université de Nantes, CNRS, Laboratoire de Planétologie et Géodynamique, UMR-6112, Nantes, France, [2]CNRS, ISTerre, Grenoble, France, [3]ISTerre, Université Grenoble Alpes, Grenoble, France, [4]Earth and Planetary Science, University of California, Berkeley, California, USA

**Abstract** We present a new surface reconstruction procedure based on the Bayesian inference method for coastal relative sea level variation during the twentieth century. Average rates are computed from tide gauge records. Models based on a Voronoi tessellation adapt to the level of information which proves well suited to the strong heterogeneity of data. Each point of the reconstructed surface is defined through a probability density function, a format particularly well adapted to this climate-related datum. The resolution of reconstructed surfaces strongly varies among the six large regions considered and within a given region. Anomalous sea level variations recorded locally are shown to reflect either anthropogenic effects or well-identified fast tectonics. For a poor data coverage, these can cause a problematic distortion of the reconstructed surface. Europe, North America, Australia, and Africa present a single trend with a decreasing precision of the reconstructed surface as a function of resolution of the tide gauge record. The most prominent feature in Europe is the pronounced uplift of Fennoscandia. Coasts of United States have the best resolution in North America and present stronger rates of sea level rise on the Atlantic than their European counterparts. Australia (especially in the North) and Africa are poorly resolved. Asia and South America depart clearly from this trend: a relatively uniform rise is obtained for Asia in spite of a good tide gauge record. Conversely, the reconstructed surface for South America presents an exceptional degree of roughness, at odds with a relatively poor record. Overall, this method not only offers a new assessment of sea level change (validating earlier results) but also quantifies the reliability of estimates.

## 1. Introduction

Recent sea level rise influenced by anthropogenic global warming since the beginning of the industrial era has a strong impact on coastal and island regions, where a significant fraction of world's population lives. The resulting concern in human societies therefore greatly enhances the scientific interests in sea level that encompass diverse fields of Earth sciences, from atmosphere to mantle dynamics.

On the Earth's surface, sea level denotes the boundary between oceans and land. As such, it is in principle a simple record that can be considered locally, on coasts, or averaged globally (Global Mean Sea Level, GMSL). The variety of time scales involved in sea level change, associated with multiple processes involving the solid Earth and the climate, often make this record difficult to decipher.

The largest contribution to sea level variations occurs on geological time scales ($10^6$–$10^9$ years) and is related to the evolution of the Earth's solid mantle flow [see, for example, *Conrad*, 2013]. The resulting changes in dynamic surface topography (including the effect of seafloor subsidence) lead to major modifications in the shape of ocean basins and are most probably the main cause for the sea level drop (more than 200 m) since the Cretaceous highstand about 100 Ma ago [*Haq and Schutter*, 2008]. However, given the rates at which those processes occur, they contribute only very little [*Moucha et al.*, 2008] to the trend of sea level in the 21st century. The main climatic effects operate on time scales of $10^6$ years and shorter. Changes in solar radiation mostly caused by Earth's orbital motion, as well as the internal variability of the ocean/atmosphere system are responsible for the twofold climatic contribution to sea level variation: the addition/removal of water from the ocean (melting/freezing of land ice from glaciers or ice sheets, or modifications in the water storage on land, including the anthropic activity) and the change of ocean water density (change in water temperature or change in salinity). In the recent past, over time scales of decades to centuries, the main reason why sea level is rising is greenhouse gases emissions from anthropogenic origin [*Intergovernmental Panel on Climate Change*, 2013]. In the 1993–present period, there is high confidence

that the two dominant mechanisms contributing to sea level rise (ocean warming, melting of glaciers) have approximately a similar amplitude and potentially explain two thirds of the record [cf. *Church et al.*, 2013].

Such a dichotomy in time scales between solid Earth and climatic processes is not operative, however, especially when local sea level change is concerned. Aspects other than global plate tectonics, yet intrinsically related to the solid Earth dynamics are important factors for the present day local sea level variation: this is the case of faster tectonic events such as earthquakes [e.g., *Broerse et al.*, 2011] or sedimentary/erosional processes [e.g., *Syvitski and Kettner*, 2011]. In addition, deglaciation is known to affect in turn the ground surface. As an elastic response, an instantaneous uplift occurs in regions where ice is melting while the absolute sea surface locally falls as a consequence of a diminished gravitational attraction typical patterns of sea level change associated with these effects are termed "fingerprints," [cf. *Conrad and Hager*, 1997; *Mitrovica et al.*, 2001; *Tamisiea et al.*, 2001]. On time scales of $10^3$–$10^5$ years, the viscous response of the solid Earth to deglaciation (Glacio-Isostatic Adjustment, GIA), results in a pattern of strong sea level fall near the formerly glaciated region and moderate sea level rise in the far field [*Farrell and Clark*, 1976]. Finally, as already indicated, these changes modify the Earth's gravitational field and, hence, its rotation [*Milne and Mitrovica*, 1998]. This further affects the geoid and the ocean surface that coincides with it over oceans.

A global measurement of sea level with high precision is available since the launch of Topex/Poseidon in 1992 (with Jason 1 and Jason 2 as successors). This satellite record, based on microwave radar altimetry, measures sea surface height relative to a geodetic reference frame. The rise in GMSL since then is $3.3 \pm 0.4$ mm/yr [e.g., *Cazenave and Llovel*, 2010; *Nerem et al.*, 2010; *Cazenave and Remy*, 2011]—the uncertainty corresponding to a statistical assessment of all sources of errors affecting satellite altimetry [*Ablain et al.*, 2009]. For earlier periods, the only available instrumental measurements correspond to tide gauges (TGs). TG stations record the superposition of the changes in sea surface height and of the vertical land motion (VLM). The latter naturally includes a GIA contribution [e.g., *Peltier*, 1998] but other causes (natural or anthropic-related subsidence, tectonic or volcanic activities) have been found to be predominant in some areas [e.g., *Wöppelmann et al.*, 2009]. VLM shall be subtracted when GMSL derived from TG record is to be compared with an evaluation from altimetry. TG stations are located on coasts and islands and thus restrict the measurement to the boundaries of oceans. TGs have first been deployed in a handful of ports in northwestern Europe at the beginning of the eighteenth century. Most TG records (including a small minority of stations in the Southern Hemisphere, $\sim$ 17%) started in the 20th century. According to TG records, the rate of GMSL rise undoubtedly increased from the nineteenth to the twentieth century and the average rise in GMSL is $1.7 \pm 0.2$ mm/yr since 1900 [*Church and White*, 2011]. This is significantly less than the value obtained for the 1993–present period by satellite altimetry. However, rates evaluated for the same recent period from TG records is of a similar amplitude as the altimetry result (yet with a significantly larger uncertainty, $2.8 \pm 0.8$ mm/yr [*Church and White*, 2011]), proving that this difference is attributable to multidecadal fluctuations of sea level rather than to an artifact related to the change in instrumentation.

Due to the spatially heterogeneous distribution of TGs and since the length of individual records is highly variable, a strong sampling bias can be expected to affect the evaluation of GMSL rise from a simple arithmetic average of sea level rates at individual TGs [cf., e.g., *Cazenave and Nerem*, 2004]. Attempts to overcome this issue include the derivation of GMSL from carefully selected TG stations with long and continuous record located in areas with no known tectonic uplift/subsidence [cf., e.g., *Douglas*, 1991] or the computation of regional averages (as done, for example, by *Holgate and Woodworth* [2004])—the most valuable approach at present possibly corresponding to the one proposed by *Jevrejeva et al.* [2006] where virtual stations are introduced from neighboring tide gauges, before performing a regional, then a global average. The high-quality data set accumulated since the beginning of the satellite oceanography era (since 1993) offers a new possibility to reconstruct earlier trends of SL rise. The spatial covariance structure obtained from the altimetry data is used to calibrate spatial functions of sea level variability (in this case, empirical orthogonal functions, EOFs [*Church et al.*, 2004; *Church and White*, 2006]) that permit to interpolate TG measurements to a global scale grid. Alternatively, EOFs can also be calibrated using numerical ocean models [*Meyssignac et al.*, 2012].

Overall, rates of GMSL obtained by these various approaches differ only slightly [cf. *Spada and Galassi*, 2012]. A more pronounced consequence of the issues mentioned above for TG records may arise when these are used to reconstruct a global spatial pattern for sea level during the twentieth century. The regional

variability in sea level rates is indeed a primordial information when trying to assess its impact on coastal areas. More accurate and reliable estimates are thus a necessary step forward for scientific and societal purposes. Some knowledge of the confidence—or probability—of the estimates would crucially improve their value.

Attempts at characterizing regional anomalies in past sea level rise have included the use of spherical harmonics [*Nakiboglu and Lambeck*, 1991] and, more recently, a technique based on neural networks where various gap-filling strategies are adopted [*Wenzel and Schröter*, 2010]. The latter approach overcomes the problems of both unknown specific weights for individual TG records and contamination by VLM, and provides regional means for sea level rates of change in eight large ocean regions. If a refined spatial resolution is sought, classical solutions involving EOFs [e.g., *Church et al.*, 2004; *Church and White*, 2011; *Ray and Douglas*, 2011; *Hamlington et al.*, 2011], although not immune from specific biases [*Christiansen et al.*, 2010], probably constitute at present the most reliable approach among the various techniques. A major issue however is that EOFs calibrated with altimetry data since 1993 might not be capable of accurately representing the spatial patterns inherent to previous decades [*Meyssignac et al.*, 2012].

Here we pursue a different goal: while the aforementioned studies based on EOFs [*Church et al.*, 2004; *Church and White*, 2011; *Ray and Douglas*, 2011; *Hamlington et al.*, 2011] sought to characterize historical sea level itself and focused on climate-related variations through the use of absolute sea level as measured by satellite altimetry, we concentrate on rates of change of sea level and restrict our analysis to coastal (relative) sea level measured by tide gauges, thus including VLM. Although once suspected to lead to higher rates [*Holgate and Woodworth*, 2004], coastal sea level rise is now considered as equivalent to global relative sea level in terms of average value for the second half of the twentieth century [*White et al.*, 2005; *Prandi et al.*, 2009]. Nevertheless, as indicated above, absolute sea level away from coasts is controlled by climate (i.e., change of water density and addition/removal of water from the ocean) and displays a typical variability in space of $\pm$ 1 mm/yr [cf., e.g., *Ray and Douglas*, 2011] while, as shown below, the variability of coastal (relative) sea level is approximately 1 order of magnitude larger since it includes VLM.

Moreover, we propose a different, new method that accounts for the heterogeneous distribution of the data set in both space and quality. These properties depend on both the density of devices along coastlines, on their record lengths, but also on the shape of coastlines. Our Bayesian approach (as in *Bodin et al.* [2012a, 2012b]) is well suited not only for technical reasons but also for the societal implications that our study aims at addressing—there is a need for probabilistic (in the Bayesian sense) rather than absolute estimates of sea level rise in threatened environments. For instance, the evaluation of economic losses [e.g., *Hallegatte et al.*, 2013] critically rely on determining the rate of sea level rise, and a probabilistic evaluation should help risk mitigation. Note that herein we focus on the tide gauges record and discard alternative geodetic devices that could yield complementary measurements after some corrections are performed (as in *Ostanciaux et al.* [2012]). Also, our results are of course indicative of relative sea level change (as opposed to absolute) because no correction is made for vertical ground motion, for our study is ultimately inclined toward risk mitigation. In section 2, we describe the data set and the simple procedure we employ to evaluate rates of sea level variations at tide gauges and associated uncertainties. In section 3, we present the surface reconstruction method and illustrate several characteristics of the procedure and of the solution in the example of Europe. Results obtained for other global regions are described in section 4.

## 2. Data Set

### 2.1. Annual Record From Tide Gauges

Tide gauge "revised local reference" (RLR) yearly data have been downloaded from the Permanent Service for Mean Sea Level [*Holgate et al.*, 2013; *Permanent Service for Mean Sea Level (PSMSL)*, 2013]. Only time series including at least 3 years of valid record (1310 stations) have been considered. Figure 1 indicates the location of these stations as well as the number of valid record ($n_{20}$) since year 1900. The strong heterogeneity between the Northern and Southern Hemispheres is obvious (1099 are located north of the equator, $\sim$ 84% of the data set). Although some stations present voids in their yearly record, it is a reasonable simplification to consider that once started, the record is continuous until present so that the number of valid record since year 1900 ($n_{20}$) is almost equivalent to the age of the station. Strong variability also affects the length of records, with 80% of stations being emplaced only in the last 50 years, and the majority of stations having record lengths shorter than 25 years. The disequilibrium between Northern and Southern Hemispheres was even more pronounced in the past: in our data set, all 44 stations with $n_{20} > 100$ are located in the

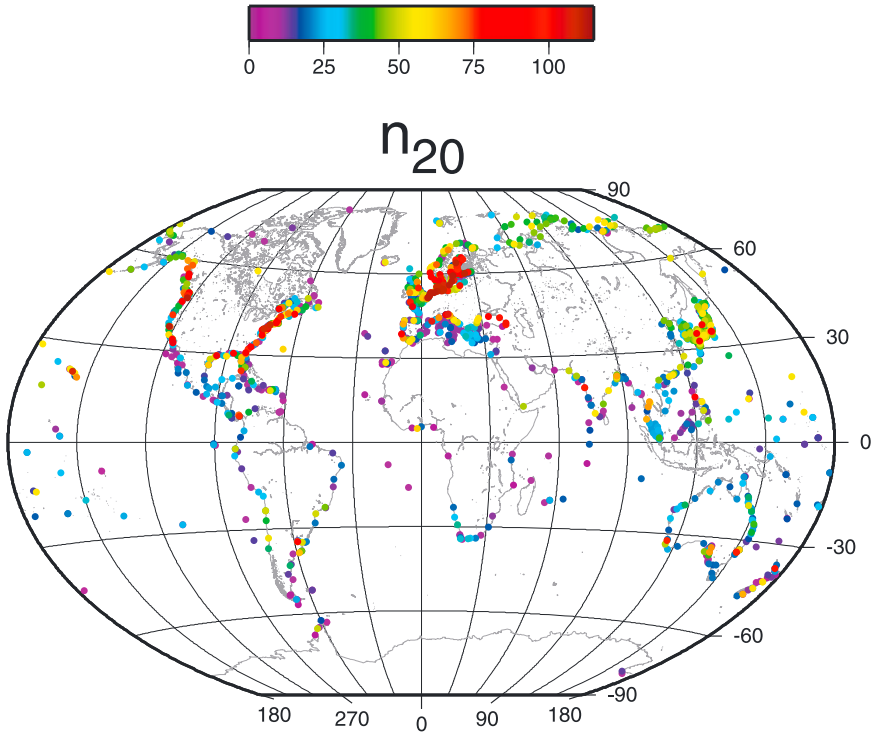


**Figure 1.** Location of the 1310 TGs considered in the present study. The color code indicates the number of valid annual records since year 1900 ($n_{20}$).

Northern Hemisphere. Among the 262 stations with $n_{20} > 50$, 92.3% are in the Northern Hemisphere—the number of tide gauges in the Southern Hemisphere exceeding 10% of the total only since ~25 years (which thus approximately coincides with the emplacement of half of the stations operating at present). It is obvious that the spatial heterogeneity will alter the surface reconstruction: a larger standard deviation is expected in the Southern Hemisphere. As shown below, this latter characteristic will be made even more prominent by the fact that, because of their globally shorter record length (the average value of $n_{20}$ is 34.3 years in the North, 22.9 years in the South), stations in the Southern Hemisphere will be associated with larger uncertainties.

### 2.2. Time-Averaged Rate of Sea Level Variation

The procedure we employ to derive the local rate $r$ of sea level variation at an individual location is based on a least squares fit of the annual RLR data set. Several attempts to detect accelerations in the rate of change of sea level have been produced [cf., e.g., *Woodworth*, 1990; *Church and White*, 2006; *Jevrejeva et al.*, 2006; *Woodworth et al.*, 2009; *Church and White*, 2011; *Houston and Dean*, 2011]. A consensus appeared to be reached on the fact that trends during the twentieth century are larger than in the nineteenth. However, conclusions on the number and dates of possible inflections during the twentieth century are still ambiguous. While most studies report an increase of the rate during the twentieth century, with possibly a short deceleration period in the early 1960s [cf. *Church and White*, 2011], other authors have observed a global deceleration since 1930 [cf., e.g., *Houston and Dean*, 2011]. Recently, *Calafat et al.* [2014] cast doubt on the reliability of such accelerations detected in the GMSL reconstructions from tide gauges: in particular, the multidecadal variability could be altered by the use of a spatially uniform EOF and may reflect regional variability.

Here we restrict our analysis to records posterior to 1900 and investigate possible variations in sea level rates of change. Two methods are considered: one where a linear fit is performed for annual data [i.e., a method very similar to the one proposed by *Spada and Galassi*, 2012] leads to rate $r_i$ and associated uncertainty $\sigma_i$ (where $i$ denotes the time range investigated); one where a parabolic fit is performed leads to the acceleration $2a$ over the period from 1900 to the present. Such a quadratic fit to individual tide gauges was already performed by numerous studies [e.g., *Woodworth et al.*, 2009; *Houston and Dean*, 2011; *Woodworth et al.*,

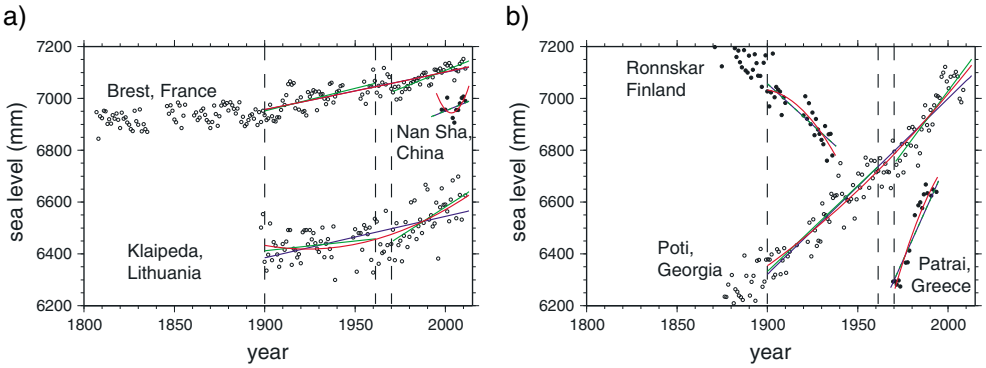


**Figure 2.** (a and b) Typical examples of linear (blue and green curves) and parabolic (red curve) fits to six RLR PSMSL data sets (noted by circular symbols, presented either filled or empty for a given TG location to avoid confusion among adjacent data sets). The vertical dashed lines underline the boundaries of the three periods considered to perform the least squares fit. The blue (linear fit) and red (parabolic fit) curves correspond to the period 1900–present (20). The two green segments indicate linear fits associated with the 1900–1961 (I) and 1970–present (II) periods. When two curves overlap (green and blue) both colors are indicated. In Figure 2b, data from Patrai and Ronnskar have been arbitrarily shifted by a constant value (−500 mm for Patrai, −400 mm for Ronnskar). The values of rates and associated uncertainties are reported in Table 1.

2011]. All the derivations introduced to evaluate the various rates and associated uncertainties are described in Appendix A. In the case of a linear fit, various ranges have been considered for time. Three examples are presented in the following, owing to their pertinence: the period from 1900 to the present (referred to as "20," e.g., as a subscript to symbols), the period from 1900 to 1961 (referred to as "I," or first part of the twentieth century), and the period from 1970 to the present (referred to as "II," or second part of the twentieth century). In the case of a parabolic fit, the period considered is always 1900–present.

Figure 2 displays several examples of fits selected for illustrative purposes. The associated values of rates of sea level variations with corresponding uncertainties are reported in Table 1 as well as the acceleration. These examples show the variety of sea level variations observed in the global data set. First, as already indicated, the record length is highly variable: $n_{20}$ is larger than 100 for Brest, Poti, and Klapeida, while it is smaller than 30 for Ronnskar, Patrai, and Nan-Sha. While Brest and Klapeida are associated to a moderate sea level rise, Ronnskar (Finland) clearly experiences the uplift of the solid Earth associated with glacio-isostatic adjustment: it is located in the vicinity (∼ 300 km) of the center of the former Fennoscandian ice sheet, and the relative sea level rate is strongly decreasing. Patrai and Poti display specific local behaviors that will be discussed below. Nan Sha records are plotted here to provide the reader with a graphical appraisal on the validity of computing rates of sea level changes from stations with short record length: here the uncertainty has the same magnitude as the inverted value of the average rate.

**Table 1.** Examples of Average Rate of Sea Level Variations for the RLR PSMSL Data Sets Displayed in Figure 2[a]

| TG # | Location | $n_{20}$ | $n_I$ | $n_{II}$ | $r_{20} \pm \sigma_{20}$ | $r_I \pm \sigma_I$ | $r_{II} \pm \sigma_{II}$ | 2a |
|---|---|---|---|---|---|---|---|---|
| 1 | Brest | 103 | 53 | 42 | 1.453 ± 0.098 | 1.74 ± 0.30 | 2.82 ± 0.25 | 0.0013 |
| 30 | Ronnskar | 28 | 28 | 0 | −6.35 ± 0.81 | −6.35 ± 0.81 | – | 0.30 |
| 41 | Poti | 101 | 54 | 39 | 6.79 ± 0.19 | 6.62 ± 0.41 | 9.40 ± 0.86 | 0.033 |
| 118 | Klaipeda | 101 | 53 | 40 | 1.60 ± 0.20 | 0.75 ± 0.42 | 4.52 ± 0.89 | 0.052 |
| 1250 | Patrai | 29 | 0 | 28 | 15.56 ± 0.76 | – | 15.55 ± 0.82 | -0.52 |
| 1730 | Nan Sha | 11 | 0 | 11 | 2.8 ± 2.7 | – | 2.8 ± 2.7 | 2.21 |

[a]The parameters [a]$n_{20}$, $n_I$, and $n_{II}$ denote the number of valid records in the periods 1900–present (20), 1900–1961 (I), and 1970–present (II). $r$, indicates the rate computed from a linear fit for each of the three periods (associated uncertainty $\sigma$). All values of rates and uncertainties are in mm/yr. Accelerations corresponding to twice the quadratic term $a$ obtained for a parabolic fit are reported in the last column (in mm/yr$^2$).

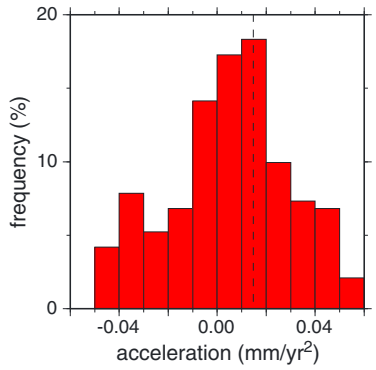


**Figure 3.** Acceleration 2*a* of sea level variation in the period 1900–present computed from a parabolic fit to tide gauge data. Only series associated with a number of valid annual records larger than 50 have been selected (246 tide gauges). Values outside the range displayed here are observed at 55 locations. The dashed vertical line indicates the average acceleration for this group of 246 tide gauges with long record lengths, 0.015 mm/yr$^2$.

The uncertainty values presented here reflect a formal error depicting the quality of the least squares fit; these are mostly related to the length of the record series: while TG stations with long series such as Brest (or Poti and Klaipeda: although much "younger," these also display an equivalent number of valid records after 1900, $n_{20} \sim 100$) have typical uncertainties $\sigma_{20} \sim 0.1$ mm/yr, shorter series such as Ronnskar and Patrai ($n_{20} \sim 30$) have uncertainties $\sim 0.8$ mm/yr, and very short series are associated with uncertainties typically larger than the average global rates (e.g., for Nan Sha, $n_{20} = 11$, $\sigma \sim 2.5$ mm/yr, note that several stations have even shorter records). Similarly, since the number of records during periods 1900–1961 or 1970–present is necessarily smaller than the number of records during the period 1900–present, the associated uncertainty is larger (note that obviously, the quality of the instrument is not considered in the computation of our formal, relative uncertainty). However, the quality of the fit also plays a (secondary) role: $\sigma_{20}$ is twice larger for Klaipeda (or Poti) than for Brest, with a similar $n_{20}$ … In the case of Brest, $\sigma_I > \sigma_{II}$ while $n_I > n_{II}$.

The parabolic approach (red curves in Figure 2) appears to be relatively poor for TGs whose record length is not long enough ($n < 30$, e.g., Nan Sha, Ronnskar, Patrai), and if not, the combination of several linear fits for different periods (blue and green curves in Figure 2) proves to be at least as efficient. We will thus focus on the rates inferred from linear fits in the following. For comparison purposes, we nonetheless report that deceleration is indeed often observed during the twentieth century at the U.S. TG stations reported by *Houston and Dean* [2011]. Not surprisingly, our values for the quadratic term 2*a* are similar although the inversion period is slightly different (1930–present for *Houston and Dean* [2011], 1900–present in this study). A global compilation of all TG records whose length is larger than 50 (Figure 3) indicates however that most of the stations present positive accelerations. The average value of 2*a* is 0.015 mm/yr$^2$, which thus confirms

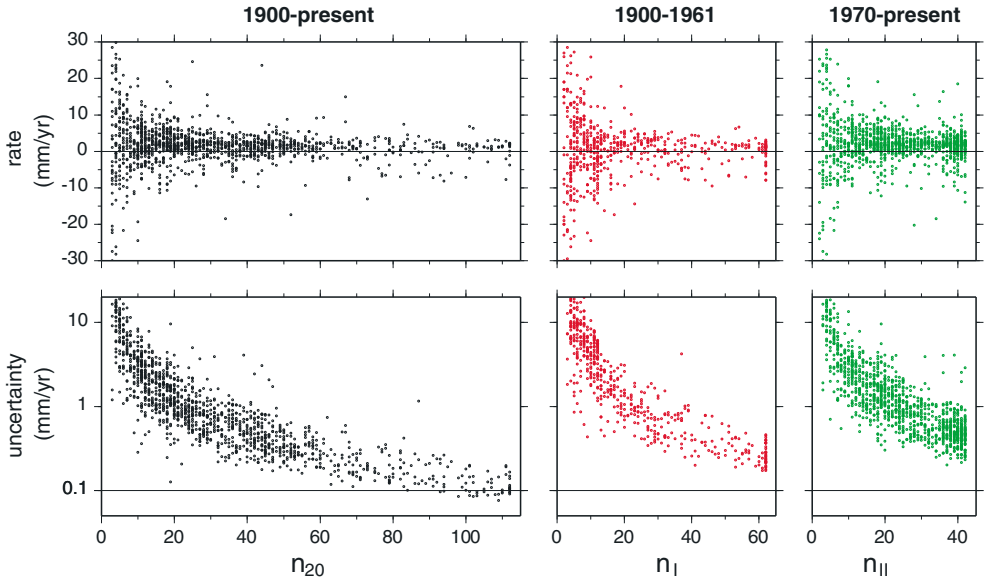


**Figure 4.** Rate of sea level variation and associated uncertainty, as a function of *n*, number of valid annual records in the PSMSL data base. Rates are computed from a linear fit to the tide gauge data. (left) 1900–present period. (middle) 1900–1961 period. (right) 1970–present period.

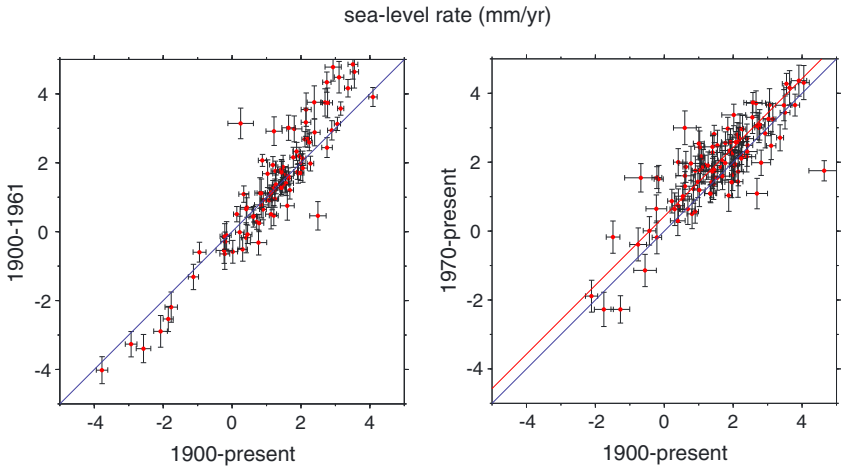


**Figure 5.** (left and right) Rate $r$ of average sea level variation (linear fit) with associated uncertainty $\sigma$ for the three different periods 1900–present, 1900–1961, (I) and 1970–present (II). Only data with $\sigma < 0.5$ mm yr$^{-1}$ have been selected (111 tide gauges). The blue and red (Figure 5, right only) lines indicate the ($y = x$) and ($y = x + 0.43$ mm/yr) curves.

qualitatively the observation of *Church and White* [2011] based on EOFs reconstructions (the fact that our data set includes stations with a potentially nonnegligible contribution of GIA does not affect acceleration values on these time scales). Note that in our case, as indicated earlier, a simple arithmetic average of accelerations at individual TGs probably includes very strong biases.

An interesting feature from Figure 2 and Table 1 is that, when it is possible to consider two periods for the linear fit (I, 1900–1961, and II, 1970–present, green curves) instead of one (1900–present, blue curve), the rate of sea level change is systematically larger for the second one than for the first one ($r_{II} > r_I$). In addition, connecting the two fits would always involve a momentary decrease of sea level during the 1960s (cf. Brest, Klaipeda, and Poti; Figure 2). This is consistent with the analysis of *Church and White* [2011] who indicate a global sea level fall of $\sim$ 10 mm between 1962 and the late 1960s. The specific boundaries of periods I and II have actually been chosen among various others (for example, involving 1930), since in our approach, these maximize the effect mentioned above when all TGs are considered.

Figure 4 summarizes the inferred rate of sea level variations as well as the associated uncertainty for the 1310 tide gauges considered in the present study. These are obtained for linear fits involving the three periods (global twentieth, I, II). Figure 4 (left) includes rates obtained for a linear fit during the "global twentieth" period (1900–present) and is therefore very similar to the one proposed by *Spada and Galassi* [2012, Figure 6]. Figures 4 (middle) and 4 (right) are associated with periods I (1900–1961, red symbols) and II (1970–present, green symbols). The distribution of $r_{II}$ (green symbols) seems globally associated with larger values than the distributions of $r_{20}$ and $r_I$ (black and red symbols). This graphical inference is confirmed by a statistical comparison of the rates among the three periods (cf. Figure 5). No clear uniform offset is observed when comparing globally period I (1900–1961) to the global twentieth period (1900–present). Absolute values of the rates are globally larger for period I ($r_I < r_{20}$ if $r < 0$, $r_I > r_{20}$ if $r > 0$). On the contrary, the rates obtained for period II (1970–present) present a systematic shift of $\sim$ 0.4 mm/yr when compared to the global twentieth period (1900–present). One single clear exception on Figure 5 (left) corresponds to the Nezugaseki station for which a strong sea level increase in 1964 has been reported as accompanying the Nigata Earthquake that suffices to explain why $r_{II} < r_{20}$ in this specific case.

As discussed in details by *Spada and Galassi* [2012], reasonable uncertainties are obtained for record lengths larger than several decades. For 262 tide gauges with large record lengths (associated with values of $n_{20}$ larger than 50), the uncertainty is systematically smaller than 1 mm/yr (a single exception, the Trois Rivières tide gauge with $r_{20} = -0.08 \pm 1.16$ mm/yr is located on the coast of the Saint-Laurent river) and the rates are in the range $[-17, 15]$ mm/yr. More precise rates might require $n_{20} > 85$ [cf. *Spada and Galassi*, 2012]… However, it is also clear that although strongly scattered, rates observed for smaller values of $n_{20}$ still present a globally positive distribution. Of the values of $r_{20}$, 76% are in the range $[-1, 4]$ mm yr$^{-1}$ and the average is $\sim$ 0.85 mm/yr. Since the relative quality of the least squares fit can be evaluated for each station,

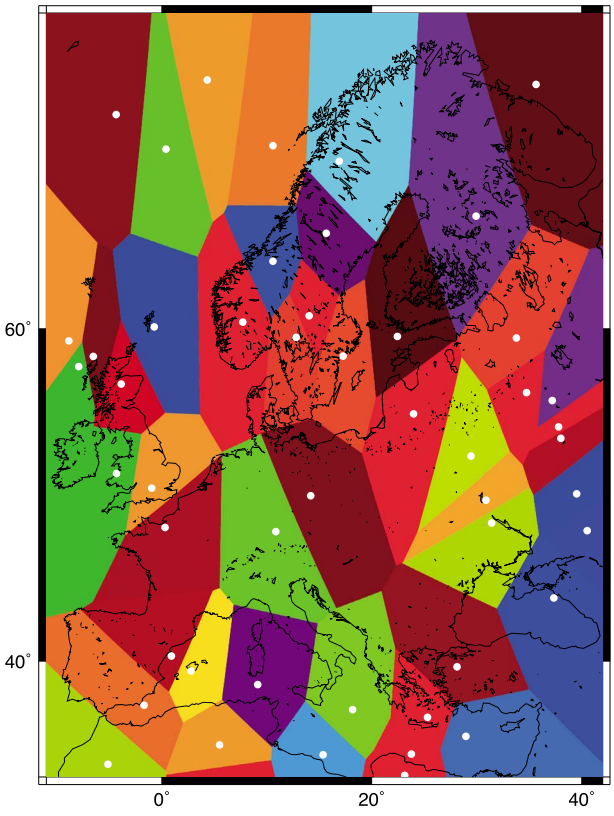


**Figure 6.** Example of initial model for the rate $r_{20}$ of average sea level variation exhibiting the Voronoi tesselation (50 cells in this model) of the surface corresponding to the "Europe" region. Any point inside a cell is closer to the node of that cell (white dot) than any other node, so the shape of the parameterization is entirely defined by the location of nodes. Boundaries between neighboring nodes are simply the perpendicular bisectors of the direct line between the center of the cells.

the probabilistic method used to compute surface reconstruction is particularly well suited for such a data set. Note that these theoretical uncertainties maybe underestimated (instrumental errors are not taken into account, nor the effect of autocorrelation among series) or obtained. Therefore, in the surface reconstruction, we ignore absolute values of these errors and only account for their relative values. In the following, we consider all the rates $r_{20}$ inferred from the 1310 TGs: while possibly unrealistically large absolute values of the rate are obtained for short record lengths, these are most frequently associated with equally large values of the uncertainty and thus will not bias the inversion procedure. Since the record lengths for periods I and II are necessarily smaller than for the global twentieth period, the uncertainties are larger (with none of the $r_I$ and $r_{II}$ values associated with a value of $\sigma$ smaller than 1 mm/yr, cf. Figure 4). These are not considered in the following of the present study.

## 3. Probabilistic Surface Reconstruction, the European Example

### 3.1. Transdimensional Regression

The ensemble of sea level rates measured at each tide gauge can be interpolated, and a continuous map for the rate of sea level rise can be constructed. A variety of algorithms is available for surface reconstruction: Generally, most 2-D regression schemes estimate surface values from weighted averages of neighboring data points. The requirement is that the surface fits the data in a least squares sense, while minimizing some global norm (e.g., level of smoothness, spline tension,...). In this way, standard interpolation algorithms often involve a few tuneable parameters, the selection of which is always a global compromise between data fit and model complexity. This results in three well-known problems:

1. The level of structure, or the roughness of the solution has to be determined by the user in advance.
2. This level of smoothness is usually spatially uniform across the surface, which prevents the solution from accounting for the uneven spatial distribution of information.
3. The arbitrary choice for a level complexity bias the solution in a statistical sense and does not allow propagation of data uncertainties toward confidence limits in the surface.

In this study, the level of information provided by tide gauge measurements is unevenly distributed geographically. As seen in Figure 1, the density of observations as well as the level of measurement uncertainties are highly spatially variable. In our case, the use of standard regression schemes is likely to either undersmooth or oversmooth subregions of the spatial domain and all the informative content of the data may not be properly utilized.

We address these issues by using an alternative approach to linear interpolation cast in a Bayesian (i.e., probabilistic) framework. The unknown model is a 2-D surface describing the rate of sea level rise. The solution is defined through Bayes theorem as the probability of the model given the observed data, namely,

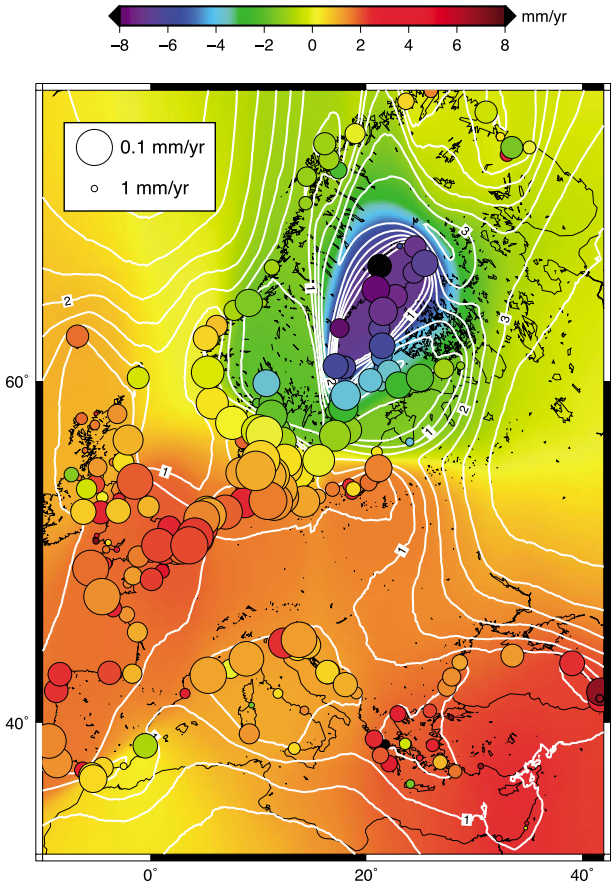


**Figure 7.** Rate $r_{20}$ of average sea level variation at 390 tide gauges on the coasts of Europe (color within circles, values lower than −8 mm/yr are in black, values larger than 8 mm/yr are in white) and reconstructed surface (color map and white contours every 0.5 mm/yr). The radius of circles indicate the uncertainty $\sigma_{20}$ as introduced above (two examples corresponding to 0.1 mm/yr and 1 mm/yr are shown on the top left corner—for clarity, results with $\sigma \geq 2$ mm/yr are not shown).

the posterior distribution [*Bayes*, 1763; *Tarantola and Valette*, 1982]. The goal here is not to describe the algorithm and its implementation in detail but instead to give the reader a general description of the procedure. For details on the algorithm, we refer to *Bodin et al.* [2012a, 2012b].

One of the advantages of using a Bayesian formulation is that uncertainties can be propagated from observations into the inferred model. Thus, the solution strongly depends on the level of data noise estimated by the user. In this study, different source of errors may affect the data and the overall level of noise may be difficult to quantify. This lack of knowledge on errors statistics can be accounted for in a probabilistic framework by using a hierarchical formulation [*Malinverno and Briggs*, 2004; *Malinverno and Parker*, 2006; *Dettmer et al.*, 2012] where the data noise is parameterized and also becomes an unknown to be inverted for in the surface reconstruction. Here we assume an independent, random Gaussian noise with a standard deviation proportional to the value $\sigma_i$ obtained from the least square procedure in previous section, with the constant of proportionality being the parameter to invert for [see *Bodin et al.*, 2012a, or details]. Further details are provided in Appendix B where we also summarize tests performed to evaluate the sensitivity of reconstructed surfaces to specific choices of parameterization for this uncertainty. These demonstrate that the evaluation of the uncertainty is appropriate, i.e., that recent tide gauges possibly recording decadal oscillations of sea level due to oceanic variability, do not contaminate the reconstructed surfaces.

The surface is parameterized with an irregular mesh consisting of a variable number of Voronoi cells [*Voronoi*, 1908] as exemplified in Figure 6. Although Voronoi cells seem complex structures, the mesh is uniquely controlled by a small number of nodes, which will be randomly perturbed at each step of the algorithm. The position and number of nodes are unknown parameters to be directly inferred from the observations. In this way, this parameterization of the surface will self adapt to the geometry of the problem. A single value of sea level rate is randomly assigned to each Voronoi cell, yielding a surface made of piecewise uniform polygons. Although this way of describing the surface seems coarse, we shall show that in a probabilistic framework the expected model tends to be a continuous surface.

Since the number of basis functions defining the surface is variable, the problem is known to be transdimensional, that is, one where the dimension of the parameter space is itself variable [*Green*, 1995; *Sambridge et al.*, 2013]. With such a transdimensional parameterization, the regression problem becomes highly nonlinear, and there is no analytical formulation for the posterior probability density function. Instead, we approximate it with a parameter search sampling algorithm (Monte Carlo), by evaluating the posterior for a large number of Voronoi models.

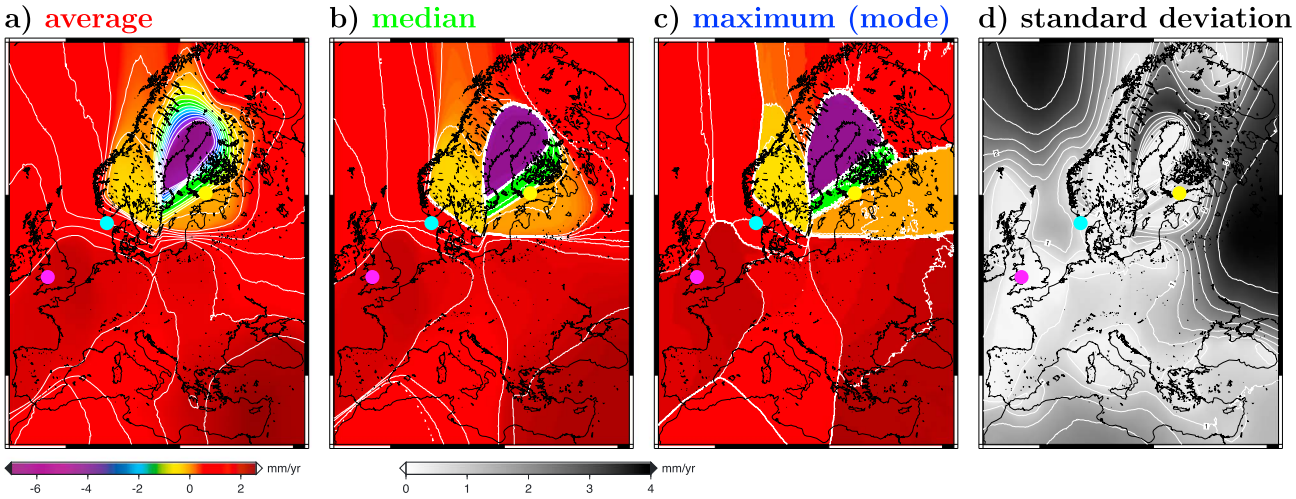


**Figure 8.** Various estimates of the reconstructed rate $r_{20}$ of sea level variation in Europe from the probability density functions at each location ((a) average, (b) median, and (c) maximum) as well as (d) standard deviation. The purple, cyan, and yellow dots indicate specific locations for which the PDF is illustrated in Figure 9.

We use the reversible jump Markov chain Monte Carlo (rj-McMC) algorithm [*Geyer and Møller*, 1994; *Green*, 1995, 2003], which is a generalization of the well-known Metropolis-Hastings algorithm *Metropolis et al.* [1953] & *Hastings* [1970] to variable dimension models. The solution is represented by an ensemble of several thousand Voronoi models with variable parameterizations, which are statistically distributed according to the posterior distribution. For a review of transdimensional Markov chains, see *Sisson* [2005].

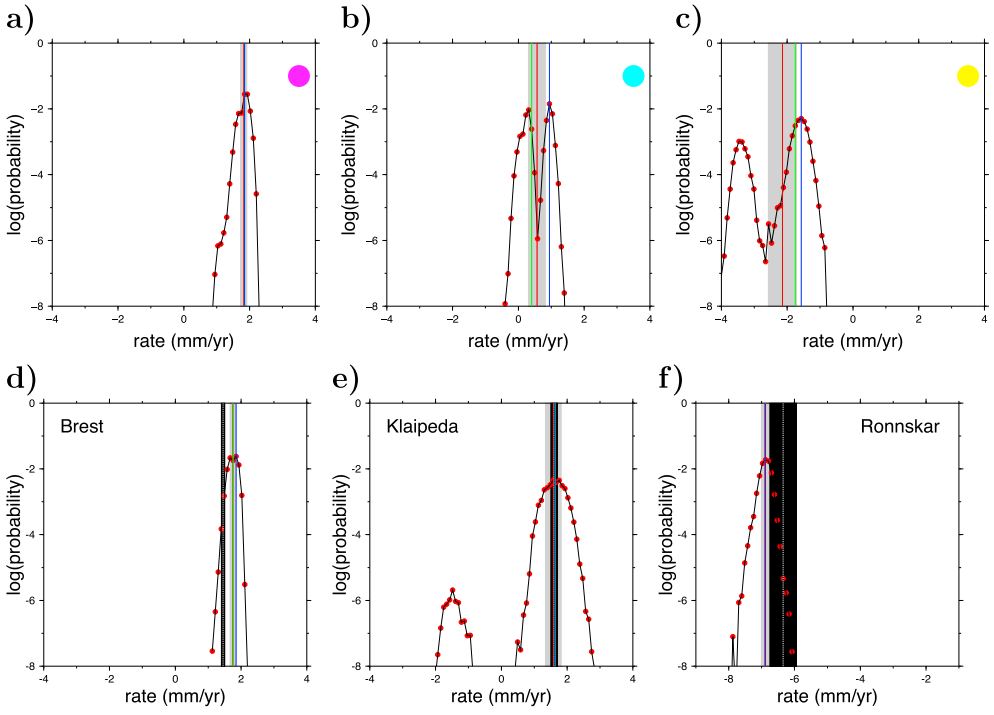


**Figure 9.** (a–c) Probability distributions at three specific locations (indicated as colored dots on the maps in Figure 8). The vertical bars denote the average (red), median (green), and maximum (blue) of the distribution. The standard deviation is also indicated as the width of the grey horizontal rectangle centered on the average of the distribution. (d–f) probability distributions at the location of three tide gauges. The colored vertical bars and grey rectangle have an identical meaning. In addition the white dotted line centered on a black rectangle indicates the initial rate and associated uncertainty computed at the tide gauge from the time series of the record.

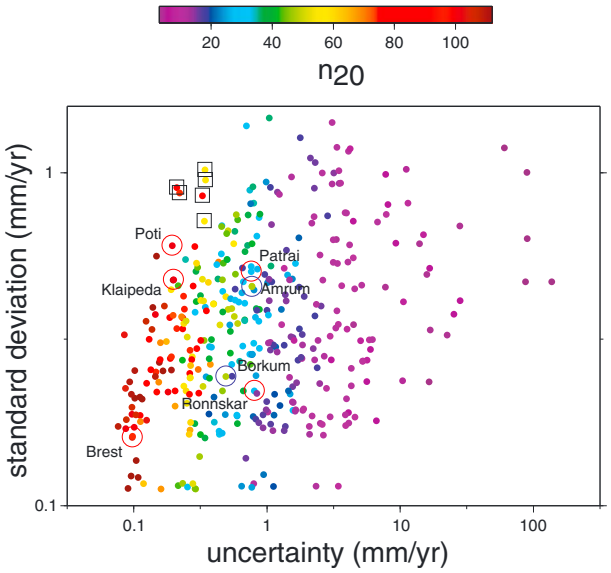


**Figure 10.** Standard deviation resulting from the probabilistic surface reconstruction at the 390 sites where tide gauges are located in Europe as a function of uncertainty $\sigma$ inferred from the least square evaluation of sea level rate $r_{20}$ from tide gauge measurements. The colors reflect the number of valid annual records since 1900, $n_{20}$. Red empty circles highlight the specific examples of the tide gauges that appear in Table 1, also discussed in the text. Blue empty circles highlight two specific stations discussed in the text. Empty squares indicate stations with a relatively large standard deviation when compared to the initial uncertainty.

For examples of applications in the Earth sciences, see *Malinverno* [2002], *Dettmer et al.* [2010], *Ray and Key* [2012], *Iaffaldano et al.* [2012, 2013], and *Tkalčić et al.* [2013].

There are a number of ways to look at this ensemble of models, for which the statistical distribution approximates the posterior probability distribution. For example, at any geographical location, the ensemble of sampled values gives a one-dimensional posterior probability of sea level rates. Thus, one can extract at any point of the map a number of statistical measures (mean, median, maximum, and standard deviation) representing the posterior distribution for sea level rate. In this way, some expected surfaces as well as a point by point error map can be constructed (see Figures 7–9). Contrary to optimization schemes, here there is no unique solution for the surface, but rather the level of information is described probabilistically, and different statistical measures can be extracted for interpretation.

The arithmetic mean (Figure 8a) is appropriate to a purely Gaussian probability density functions (PDF), whereas the median (Figure 8b) is a robust statistic that can be effectively applied to a wide range of PDFs. The map for the mode (maximum) in Figure 8c has the most distinctive character, as it tends to preserve the sharp jumps of the underlying Voronoi models. Finally, the standard deviation (Figure 8d) can be seen as an error map for the expected surface. For more details about transdimensional regression, we refer the reader to *Bodin et al.* [2012a].

### 3.2. Interpreting the Probability Density Functions

Figure 9 also displays the full probability density functions at six specific locations: three of these (Figures 9a–9c) are chosen among regions where the standard deviation is smaller than 1 mm/yr (these are not located directly on the coast), three correspond to tide gauges Brest, Klaipeda, and Ronnskar (Figures 9d–9f, respectively).

The purple dot (Figure 9a) is an example from an area where the PDF shows a small standard deviation ($<$ 0.19 mm/yr), where the median and the maximum are identical (1.84 mm/yr) and very close to the average (1.82 mm/yr). Note, however, that the PDF is asymmetrical and, as discussed below, could possibly be envisioned as the superposition of several Gaussian type distributions. At the location of the cyan dot (Figure 9b), a bimodal distribution is clearly observed. If modeled with the superposition of two normal distributions, the one on the right would have a slightly smaller mean and a slightly larger variance. As a result, the maximum of the global PDF is larger than the average, itself larger than the median (the standard deviation is 0.52 mm/yr). Again, the PDF associated with the yellow dot (Figure 9c) is bimodal with a global maximum at −1.58 mm/yr and a second local maximum located near −3.5 mm/yr. In this case, the average is smaller than the median. Although the smaller peak is approximately twice less probable than the largest one, both are relatively distant, which leads to a standard deviation of 0.86 mm/yr.

The multimodal character of the PDFs is a consequence of our choice for the parameterization of models based on the Voronoi tessellation, which thus induces regions with uniform values of the sea level rate: Peaks in the PDFs at a given location reflect the presence of tide gauges in the neighborhood

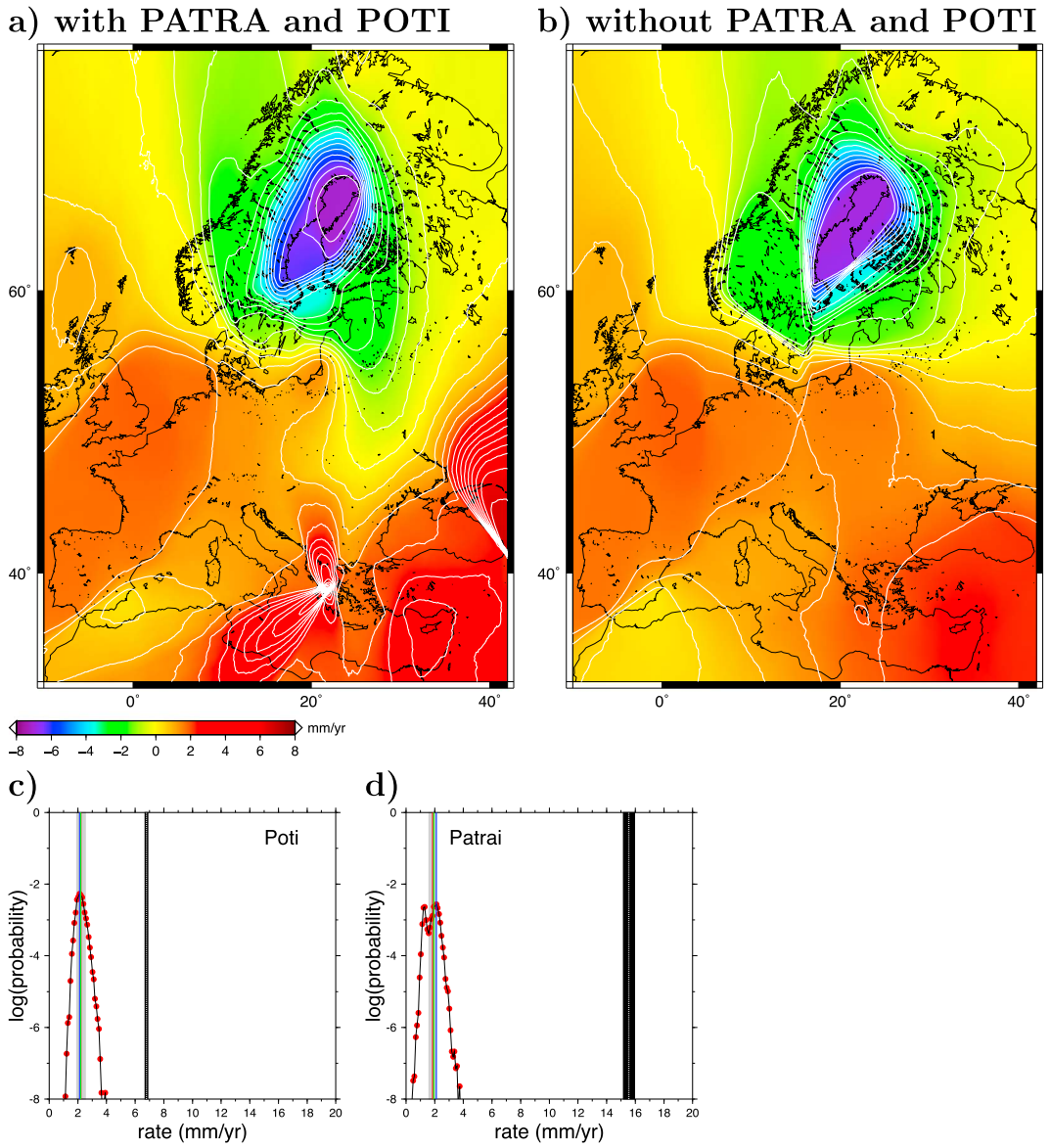


**Figure 11.** Influence of two outliers (TG stations Patra and Poti) on the surface reconstruction. (a) Surface reconstruction taking into account the two outliers. (b) Surface reconstruction discarding the two outliers. The color code is identical to the one in Figure 7. In the case where the two outliers are not included in the surface reconstruction procedure, Figures 11c and 11d display the probability distributions at the location of each outlier. Again, vertical bars denote the average (red), median (green), and maximum (blue) of the distribution. The standard deviation is also indicated as the width of the grey horizontal rectangle centered on the average of the distribution. In addition, the white dotted line centered on a black rectangle indicates the initial rate and associated uncertainty computed at the outlier tide gauge from the time series of the record (not considered for surface reconstruction).

(either because these are in the direct vicinity or because their associated uncertainty is small enough to extend their radius of influence up to this location). We note that regions where PDFs display a multimodal behavior are sparse and mostly located where large gradients of sea level rate occur, for instance at the margins of the former Fennoscandian ice sheet in the case of Europe. A different result would then have been obtained if more precise functions (such as splines or some polynomial equivalent) had been used in the models. We emphasize however that multimodal distributions are able to fully describe the level of available information in areas with conflicting tide gauge records.

Figure 9d displays the PDF obtained at the precise location of the Brest (France) tide gauge. Thanks to the long and coherent record at this station and the relative homogeneity of measurements in the area,

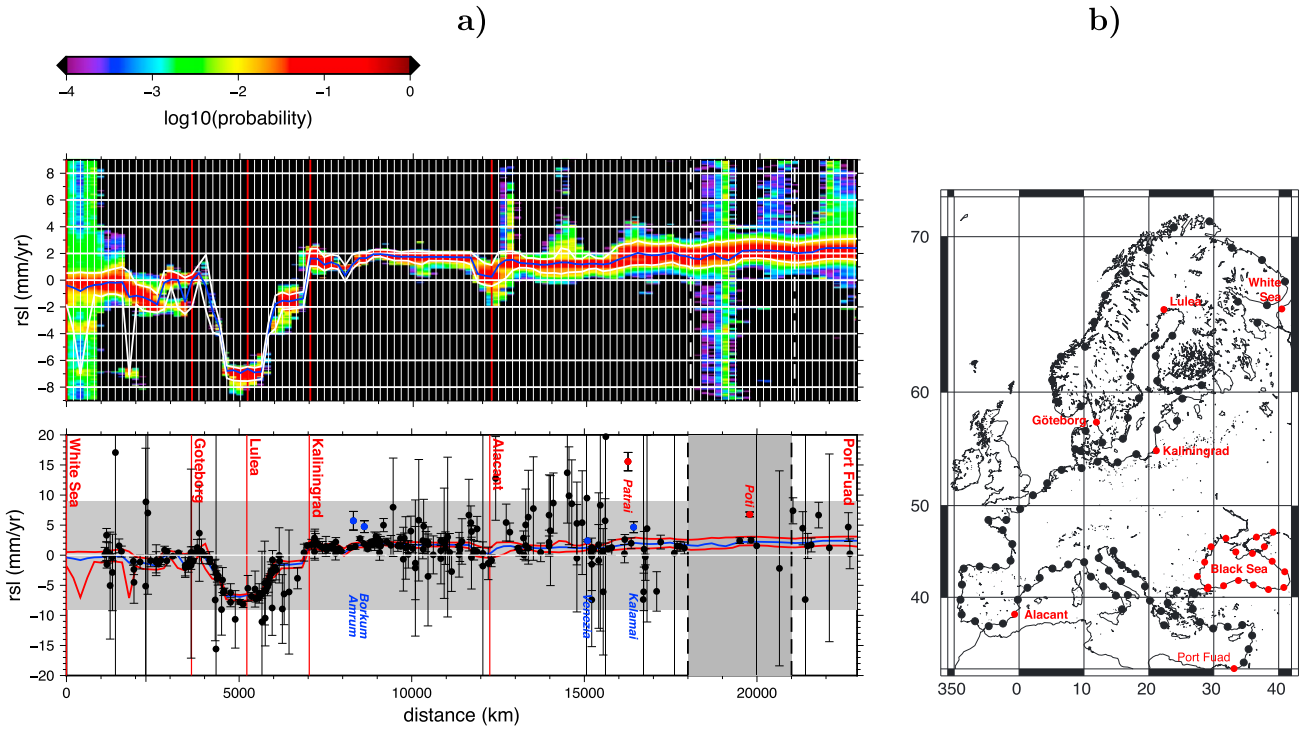


**Figure 12.** (a, top) Probability density function for rate $r_{20}$ of average sea level variation along the coasts of Europe. The blue line indicates the mean of the distribution at each location. The two white lines show the 95% credible interval. (a, bottom) Average and standard deviation (same as above) as well as rates and uncertainties computed at tide gauges (black circles with error bars). The grey shaded rectangle indicates the range used for sea level reconstructions. The two red circles highlight the two outliers discussed in the text. The four blue circles highlight anomalous stations (i.e., stations with an uncertainty smaller than 2 mm/yr that lie out of the confidence interval of the reconstructed surface). (b) Locations of the 113 samples used to produce the posterior distribution (indicated on Figure 12a) as thin white vertical lines). Red dots and associated names are explicitly reported on the profile of Figure 12a.

the standard deviation is among the smallest in our reconstruction (0.16 mm/yr) and the median and maximum of the PDF both lie within 0.10 mm/yr of the average value (1.75 mm/yr). We note however, that the reconstructed distribution peaks at a slightly larger value than the rate directly inferred from the time series (1.45 mm/yr, see Table 1). This could reflect a specific local behavior of sea level near Brest, but, more likely, this results from varying lengths in the tide gauge records: all of the stations neighboring Brest present shorter record lengths and thus associate a larger weight to the recent increase of sea level rise during the satellite era. Exceptionally good tide gauges, although they force the reconstruction in a more decisive way thanks to the smaller associated uncertainty, are still affected by the surrounding stations with number of valid yearly records $n_{20}$ corresponding to several decades.

The Klaipeda tide gauge, in Lithuania, also presents a long record with a small uncertainty (cf. Table 1). Figure 9e indicates that, again, a small standard deviation is associated with the reconstructed PDF (0.48 mm/yr) and the maximum and median are less than 0.05 mm/yr apart from the average (1.58 mm/yr). In this case, the PDF is almost exactly centered on the rate initially inferred from the tide gauge (1.60 mm/yr). Contrary to Brest, Klaipeda has few neighboring stations with sufficiently long record to be able to influence the reconstruction (cf. Figure 7): $n_{20} = 52$ for Kaliningrad (located $\sim$ 100 km south) but the rate inferred from tide gauge data is similar (1.76 mm/yr); $n_{20} = 26$ for Liepaja (located $\sim$ 100 km north) with a negative rate, probably explaining the secondary (25 times less probable) local maximum in the PDF. The case of Ronnskar (a Swedish island located $\sim$ 30 km west of the coasts of Finland) is also illuminating since the reconstructed PDF (Figure 9f) is again quite sharp (standard deviation of 0.22 mm/yr) but displays an average value (−6.90 mm/yr) that is noticeably smaller than the rate inferred from the tide gauge date (−6.35 mm/yr). In this region of the Baltic Sea, the most significant feature is the large gradients of sea level rate induced by the GIA.

The quantitative effect of the surface reconstruction is well illustrated by the comparison of the standard deviation obtained a posteriori at the locations of tide gauges where the uncertainty $\sigma$ measuring the

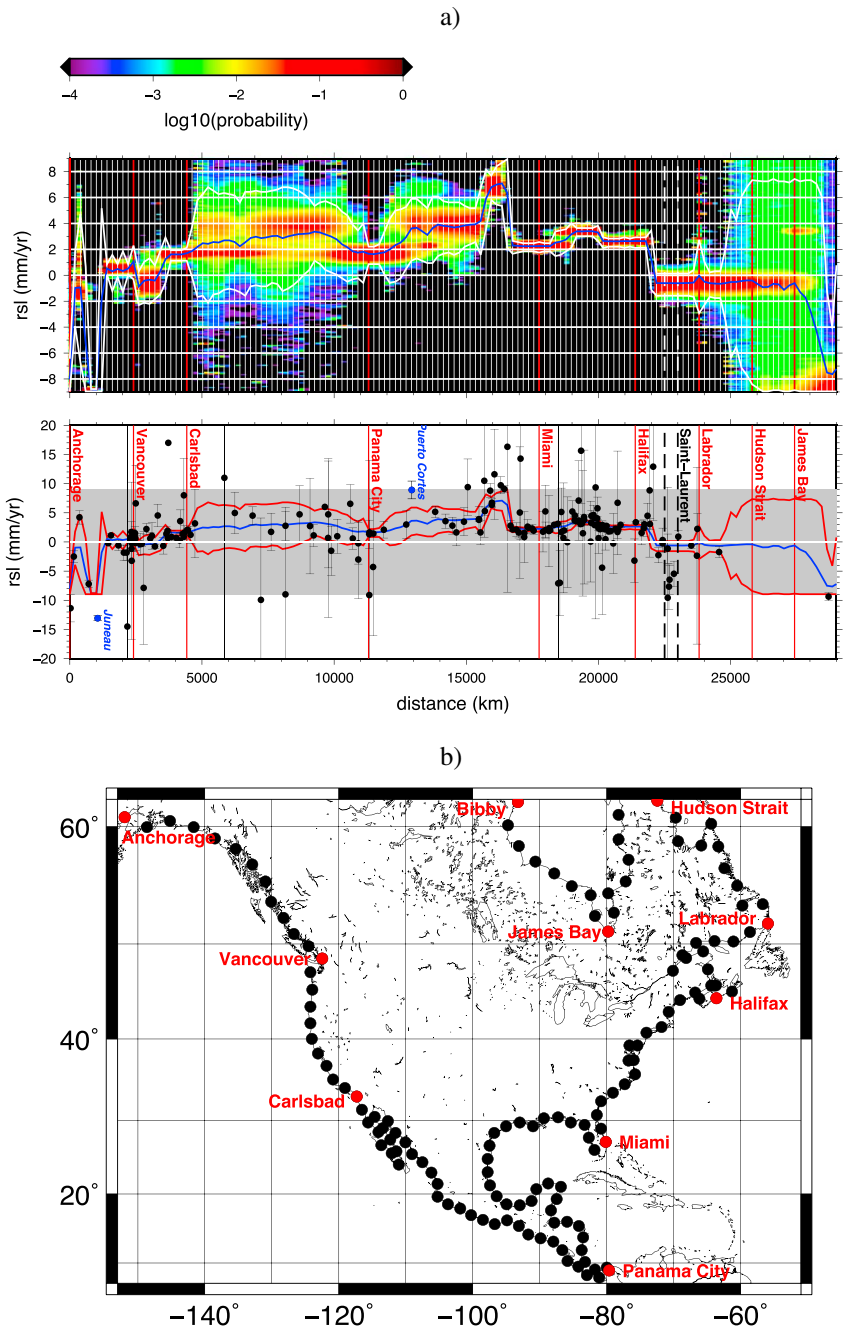


**Figure 13.** Same as Figure 12 for the coasts of North America.

quality of the least squares fit used to evaluate the sea level rate $r_{20}$ is also available a priori (Figure 10). Note that both quantities cannot be directly compared as values: the uncertainty $\sigma$ is a strictly local measurement that reflects mostly the length of the tide gauge record (with a less important effect due to the noisiness of the sea level rate on the considered period). It is based on a 95% confidence interval. The standard deviation mostly reflects the error on the reconstructed surface which includes effects of the parameterization (cf., e.g., models based on Voronoi cells) as well as the spatial structure of the data set (cf. discussion on Figures 9a–9f, see also section 3.3). Furthermore, as seen above, different gauges measure the sea level rate across different time ranges. In the case of a nonlinear trend, this may imply inconstant rates between neighboring stations, which is accounted for by an increased standard deviation. This interval accounts for ~68% of the PDF (95% would correspond to twice this value). Nevertheless, both quantities can be understood in

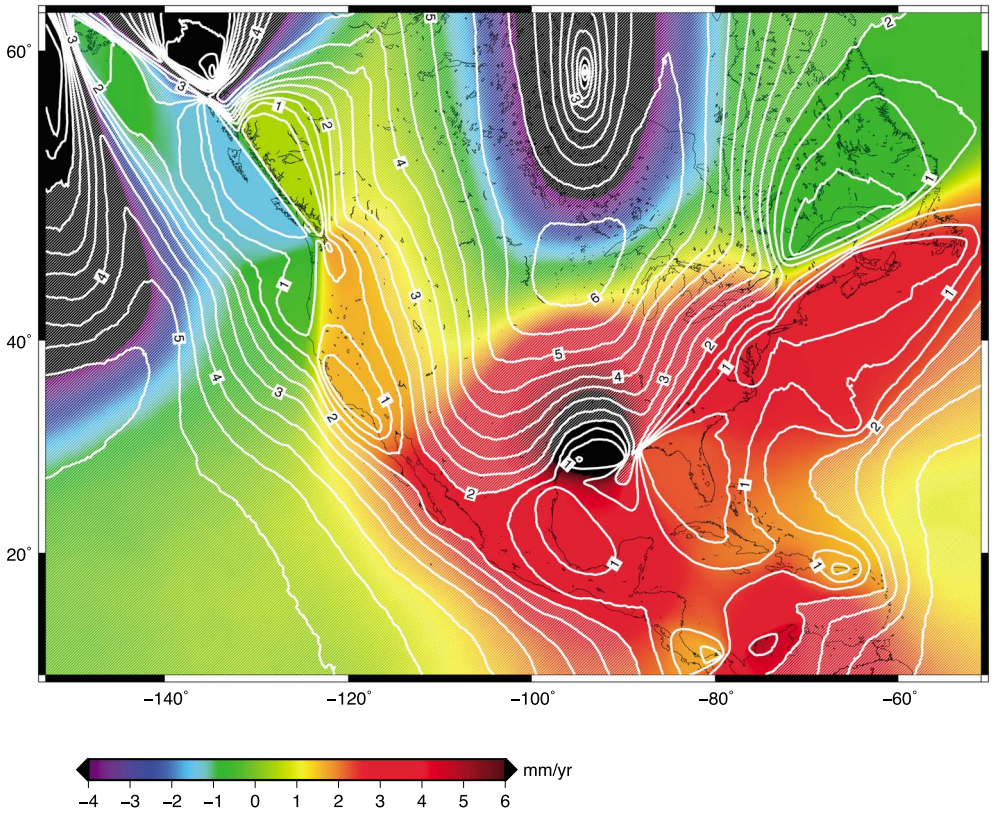


**Figure 14.** Reconstructed surface for rate $r_{20}$ of average sea level variation in Northern America. The color code depicts the average of the probability density functions. White contours indicate isovalues of the standard deviation (with a 0.5 mm/yr interval). Zones where the standard deviation exceeds 2 mm/yr are hatched by thin white lines.

terms of a single concept, termed "error" in the following. In Figure 10, the specific results discussed above for Brest, Klaipeda, and Ronnskar are illustrated in a simple way. A global outcome is that the probabilistic reconstruction reduces the amplitude of the error: while many locations were initially associated with a very large uncertainty (> 3 mm/yr, always associated with few annual records, $n_{20}$ <15), the maximum standard deviation is less than 1.5 mm/yr. Most of the time, cases where the standard deviation exceeds the initial uncertainty are associated with tide gauges with a large number of annual records and thus to small values of the uncertainty (this is the case for stations Brest and Klaipeda described above). The handful of stations where the probabilistic reconstruction could be considered to have worsened the error, highlighted by empty squares on Figure 10 are all located on the margins of the Fennoscandian uplift, where the gradient in the rate of sea level change is the highest (Figures 8a–8c). The many Voroinoi tessellations yield as many maps where the sharp transition from the more stable Europe to the fast uplifting Fennoscandia is laterally offset by short distances, yet causing the PDFs to quickly disperse.

### 3.3. Outliers

While our goal is to exhibit sea level variations that include VLM, very localized signals associated to tectonics or anthropogenic activity can distort the reconstructed surface. If the density of tide gauges surrounding such anomalous records is large enough, these do not alter the reconstructed surface (see below). In specific areas with relatively poorer data coverage, such anomalies impair the reconstruction. Our method tends to minor the influence of irrelevant data points, whose weight degrades either because of the short duration of their record or because of the noisiness of the record. In principle, the procedure does not require manual intervention for this entirely automated method. But a glance at the European example immediately calls for suspicion (Figure 11a): two stations, Poti (Georgia) and Patrai (Patrai, Greece), feature rates of sea level change that significantly depart from the long wavelength trends by factors ~3 and ~8, respectively. Because they are considered reliable (cf. Table 1), for their record lengths and noisiness are excellent, they force the global interpolation by imposing high-frequency variations.

**Table 2.** Global Characteristics of the Six Large Regions Considered in This Study[a]

| Region | Area ($\times 10^6$ km$^2$) | $l_{coasts}$ ($\times 10^3$ km) | $n_{TG}$ | $n_{20}^{cum}$ (yr) | $N_{cell}$ | $res_A$ ($\times 10^3$ km$^2$/yr) | $res_l$ ($\times$ km/yr) | $A_{cell}$ ($\times$ km$^2$) | $\lambda_{cell}$ ($\times 10^3$ km) |
|---|---|---|---|---|---|---|---|---|---|
| Africa | 68.2 | 25.5 | 112 | 2,013 | 5.11 | 33.9 | 12.6 | 13.4 | 3.66 |
| Asia | 46.5 | 19.1 | 292 | 8,990 | 5.06 | 5.17 | 2.1 | 9.19 | 3.03 |
| Australia | 17.9 | 13.1 | 75 | 1,980 | 6.96 | 9.05 | 6.6 | 2.57 | 1.60 |
| Europe | 16.4 | 22.9 | 390 | 14,800 | 32.4 | 11.1 | 1.5 | 0.508 | 0.713 |
| North America | 55.1 | 29.0 | 279 | 9,520 | 31.2 | 5.79 | 3.0 | 1.77 | 1.33 |
| South America | 38.6 | 22.6 | 59 | 1,490 | 56.5 | 25.9 | 15.1 | 0.684 | 0.827 |

[a]The parameter $n_{TG}$ is the number of tide gauges involved for a given region. For example, in the case of Africa, this number includes a significant number of stations located on the northern shores of the Mediterrenean, see Figure 18. The parameter $n_{20}^{cum}$ is the sum of the record lengths of all tide gauges involved in the surface reconstruction for a specific region. $N_{cell}$ is the average number of Voronoi cells in the surface reconstruction models. The parameters $res_A$ = area/$n_{20}^{cum}$ and $res_l$ = $l_{coasts}/n_{20}^{cum}$ give a measure of the resolution provided by the tide gauge record in a given region (the unit is meaningless here). $A_{cell}$ and $\lambda_{cell}$ are respectively the typical area and typical lengthscale of Voronoi cells.

Patrai reveals the importance of local tectonics. It is located in the eponym rift, an arm of the Corinth rift that connects to the Kefalonia fault, to the West [e.g., *Royden and Papanikolaou*, 2011; *Vassilakis et al.*, 2011; *Guillaume et al.*, 2013]. Seismic surveys depict a tectonically driven subsidence of several mm/yr [*Ferentinos et al.*, 1985; *Chronis et al.*, 1991] that is confined in the fast opening Patrai rift. The exceptional tectonic rates are very localized yet representative of an ongoing process.

The case of Poti [*García et al.*, 2007; *Stanev and Peneva*, 2001] is emblematic of another source of local peculiarity that drives fast subsidence: Here the tide gauge is located in the Kolkheti lowlands, in Georgia, where ground level is controlled by sediment discharge at the mouth of several rivers including the Rioni river. The successive swamps, mires, peatlands, and bogs record the evolution of the very fragile equilibrium, easily altered by slight external forcings, the greater being anthropogenic [*de Klerk et al.*, 2009, *Kereselidze et al.*, 2011]. Intensive drainage in the twentieth century deprived the delta from the sediment input, which caused subsidence in a comparable situation to that of many deltas like the Brahmaputra mouth, where sediment starvation jeopardizes the fate of Bangladesh.

In both cases, the impact of these local features is well illustrated by the general map (Figure 11b) but also by their PDFs (when their role is discarded from the surface reconstructions) when compared to the rate inferred from the time series (Figures 11c and 11d). The discrepancy between the locally derived rate and the average values for the PDFs amounts to ~5 mm/yr (Poti) and ~13 mm/yr (Patrai). Yet both the standard deviations and local uncertainties are robust (< 0.5 mm/yr). Here in the case of Patrai or Poti, the anomaly pokes out of the map.

### 3.4. Probability Density Function Along the Coasts

Ultimately, the tide gauges record only documents sea level variations on coastal regions. For this reason, Figure 12 displays both the full PDFs along the coasts of Europe and the initial rates and associated uncertainties inferred from the least squares fit of tide gauge data. It gives a clear summary of the analysis developed in previous sections for this specific data set: first, our procedure obviously fills out the gaps where tide gauges are lacking or are associated with short record lengths (e.g., distances smaller than 1000 km, corresponding to the coasts of the White Sea and the Barents Sea, as well as distances larger than 15,000 km, corresponding to the Eastern part of the Mediterranean and the Black Sea). It also helps to discriminate between conflicting measurements recorded by tide gauges in a densely covered region (this is the case of Western Europe), providing a smooth description in these areas. This either leads to a smaller error than estimated by stations with short record lengths or indicates local deviations from the expected surface. Three examples clearly stand out between distances 8000 and 9000 km and at distance ~16,500 km (blue circles), corresponding to stations Amrum and Borkum in Germany and Kalamai in Greece—these stations are known to present anomalies, cf. *Holgate et al.* [2013] and *PSMSL* [2013]. Similarly, the Venezia (Punta della Salute) tide gauge (at distance ~15,000 km) lies out of the confidence interval. It is discussed below (see section 4.1). These anomalous stations do not influence the surface reconstruction since it is tightly

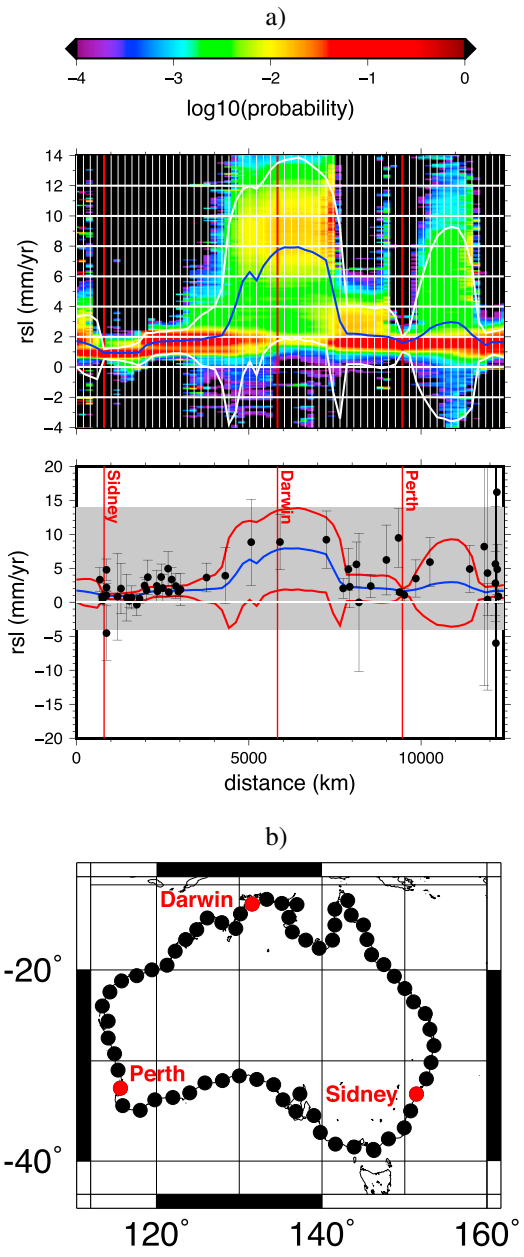


**Figure 15.** Same as Figure 12 for the coasts of Australia.

constrained by other reliable measurements in the vicinity of such stations. This is not the case of the two outliers, Patrai and Poti that have been excluded from the surface reconstruction: Figure 12 further shows that the surface is not sufficiently constrained in these areas to be immune from such anomalies. An interesting feature is that several stations between distances 12,000 and 16,000 km (between Alacant and the eastern part of the Adriatic Sea) seem to depart from the reconstructed surface, generally associated with larger rates of sea level rise, although uncertainties are large. A specific focus on each station would help constrain the origin of such a behavior. Finally, the multimodal PDFs described above are confirmed to be quite rare. These are restricted to the northernmost part of Europe and in a small region near Alacant.

Overall, our method provides a powerful illumination of the tide gauge data set, minimizing the error in locations with few surrounding stations and even reducing it at numerous tide gauges where the record length is small. Slightly problematic regions are restricted to the margins of the Fennoscandian uplift where gradients of relative sea level rise caused by the GIA are largest.

## 4. Global Results

In the following, we deploy our method to six regions that overall encompass most coastlines. We analyze our results on the basis of their predictive quality, focusing on some specific areas of high interest or risk and, when possible, we decipher the mechanisms that are involved. Note that we represent the reconstructed surfaces on the whole region (Figures 14, 16, 18, 20, and 22) although tide gauge records only enable ultimately to illuminate coastal sea level (offshore climatic effects are not recorded and since relative sea level is not restricted to VLM, its extension to continental regions is not straightforward): regions where the standard deviation is large are hatched with thin white lines. In order to properly interpret our results, one needs to go beyond the mean value and explore a variety of metrics, taking full advantage of the PDFs obtained in the surface reconstruction.

### 4.1. Europe

The tide gauge record in Europe yields the most favorable conditions to apply our method. The data coverage is fine, and record lengths are the longest available (frequently yielding low local uncertainties), with the best cumulated record length of all stations and resolution per unit length of coastline (Table 2). In addition, although stations are only located on coastlines, the sinuous geographical distribution of the shores of the Mediterranean, Atlantic, British Isles, Baltica, and Fennoscandia, together with the high density of stations, provide a relatively homogeneous sampling of the region (Figure 1). Consequently, the average number of Voronoi cells in the surface reconstructions is high (32.4) and the PDFs are very good (Figure 12),

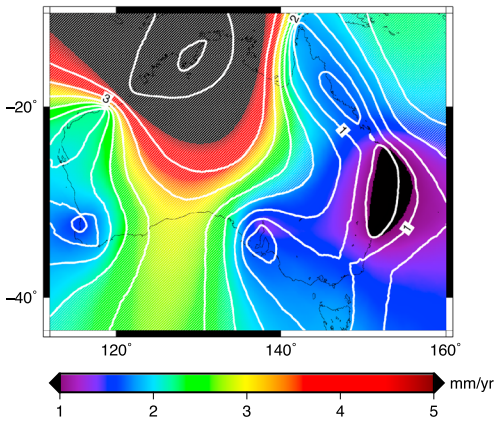


**Figure 16.** Same as Figure 14 for Australia.

although these slightly deteriorate in the south (the standard deviation increases from values that are typically lower than 0.5 mm/yr to ∼1 mm/yr).

The most prominent feature is, as expected, the fast sea level drop centered in Baltica with a rate of ∼−7 mm/yr, a value that quickly drops to ∼−1.5 mm/yr along the coasts of the North Atlantic to the west, but also toward the European hinterland to the east and south and toward the Arctic. Outward from the Baltic sea, this relative sea level drop decreases extremely fast (more than 1 mm/yr per hundred kilometers). Clearly, this signal relates to the prime mechanism of glacio-isostatic adjustment (GIA), i.e., the elastic rebound of the lithosphere that accompanies the Holocene deglaciation. In order to reach such values, uplift rates must significantly overcome sea level rise. Indeed, these values compare well to the estimate of land uplift, as measured from a variety of devices [see, e.g., *Ostanciaux et al.*, 2012, for a review].

The signal is fairly sharp in western Europe too (standard deviation does not exceed 0.5 mm/yr), where subsidence occurs uniformly at a rate of 1.5 to 2 mm/yr from Kaliningrad to Alacant (Figure 12); it slightly exceeds sea level rise, and the viscous terms of the GIA may here control the subsidence along this coast where vertical ground motion is negative [e.g., *Ostanciaux et al.*, 2012; *Serpelloni et al.*, 2013]. It must be noted that the tide gauge of Brest (at distance ∼ 9700 km, Figure 12), which is associated with one of the smallest uncertainties ($r_{20}$ = 1.453 mm/yr, $\sigma_{20}$ = 0.098 mm/yr, cf. Table 1), is very close to the lower end of the range while still lying within the confidence interval of the reconstructed surface (mean value: 1.76 mm/yr, width of the 95% confidence interval: 0.65 mm/yr). As indicated earlier, this is because neighboring records span smaller time intervals, almost always corresponding to more recent periods. The weight of the most recent era, coinciding with the satellite record and associated with an accelerated sea level rise is therefore larger in the reconstructed surface. It is quite comforting however to note that this bias does not exceed the confidence interval there. Further east in the Mediterranean, subsidence may decrease to slightly more modest values (∼ 1 ± 0.5 mm/yr) in the Western Mediterranean and increases again toward the Aegean sea. Around Italy, we note that vertical ground motion as interpreted from GPS measurements by *Serpelloni et al.* [2013] varies spatially much quicker than suggested by the results of our interpolation. Overall, the rates in Southern Europe (typically ∼ 1–2 mm/yr) are compatible with the sea level rise as measured from satellite altimetry [e.g., *Cazenave and Llovel*, 2010], possibly further reenforced by a contribution from postglacial rebound (see GIA reconstructions from G. Spada in *Serpelloni et al.* [2013], for instance), but the tradeoff is difficult to decipher a priori.

In Europe, some places are critically exposed to sea level rise, typically like the Netherlands (subsiding at ∼2 mm/yr) or the Po plain and Venezia (subsiding at a rate of more than 2 mm/yr), and many other Mediterranean cities that are threatened by major economic losses in the near future [*Hallegatte et al.*, 2013]. In the first case, our method clearly confirms the robust measurements and assigns them a regional validity. In the second case of Venezia, the standard deviation is much lower than the typical uncertainties at tide gauges in the Po plain although it clearly departs from the local trend (e.g., the nearby Trieste tide gauge, with a twice smaller rate of subsidence, lies typically in the confidence interval). We consider that this specific feature of the reconstructed surface shows that while our approach may be considered as a powerful tool helping to quantify a regional trend precisely, it also helps to highlight anomalous results (caused here by prominent anthropogenic forcings in this area that prove to be only local and unambiguously anthropogenic): due to the overall quality of the data set, local departures from the regional trend will be considered as noise in our model even if associated with small uncertainties (as is the case also for anomalous stations Amrum and Borkum corresponding to the blue dots in Figure 12).

### 4.2. North America

North America offers almost as good conditions as Europe to deploy our method: the data coverage and record lengths are fairly good which yield an average number of Voronoi cells that compares to the

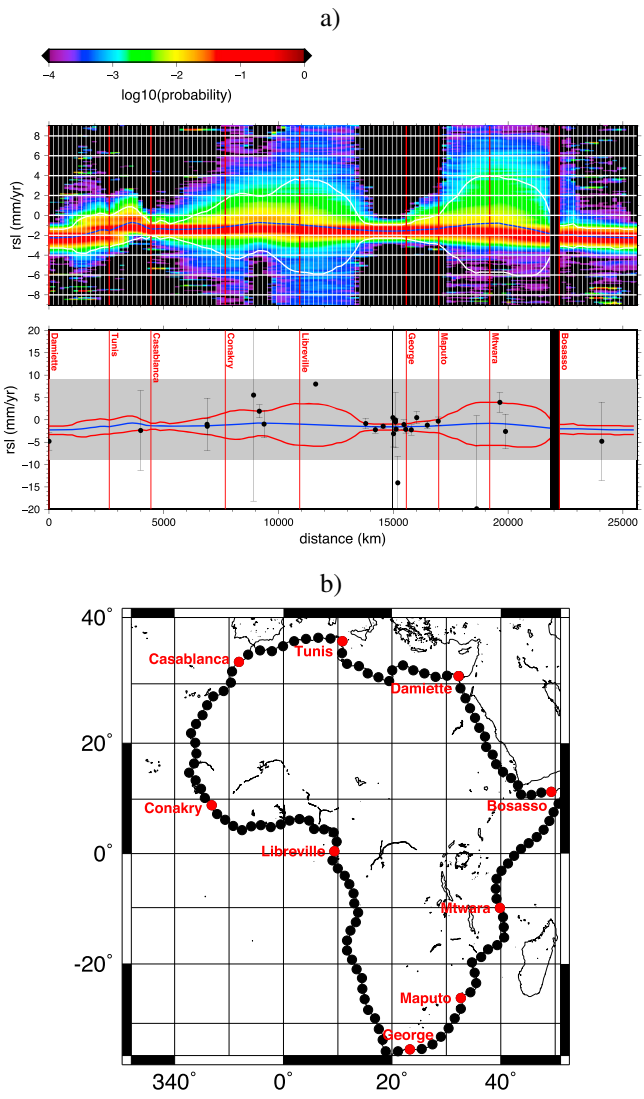


**Figure 17.** Same as Figure 12 for the coasts of Africa.

case of Europe, with relatively small cells and good mean resolution (Table 2). Uncertainties are therefore low and only in the Arctic and to a lesser extent Mexico and Central America, does the quality degrades (Figures 13 and 14). The standard deviation along most of the East and West coasts of Canada and United States (between Alaska and Carlsbad, and between the Mississipi and the Labrador) is lower than 0.5 mm/yr (Figure 14). From south to north along the East coast, and within a 95% confidence, Florida subsides at rate of $2.2 \pm 0.3$ mm/yr, a value that increases to $3.5 \pm 0.3$ mm/yr in North and South Carolina, before decreasing to $\sim 2.5 \pm 0.3$ mm/yr in New England. In this context, it must be emphasized that coasts in the northwest Atlantic are typically associated with a larger sea level rise than northeast Atlantic regions. This confirms the result obtained by *Long et al.* [2014] from the Newton salt marsh located in the central English Channel: these authors demonstrated that the abrupt acceleration recorded by several salt marshes in the northwest Atlantic region which occurs in the late nineteenth or early twentieth century, and is used to calibrate models of global climate and sea level [e.g., *Rahmstorf et al.*, 2012], is not observed on European coasts. Some of these areas are critically exposed to this fast relative sea level rise and policy makers and risk mitigating crucially rely on trustworthy assessments. This is obvious for instance in North Carolina [see, e.g., *Kemp et al.*, 2011, and discussions thereafter]; similarly, Miami, New York, New Orleans, Tampa, and Boston rank within the top 20 cities for which the cost of potential damages are the highest [*Hallegatte et al.*, 2013].

Relative sea level flips to a $\sim -0.8 \pm 1$ mm/yr uplift by the mouth of the Saint-Laurent, a relative uplift that increases to some 7 mm/yr in the Hudson Bay. Such a fast uplift is due to the GIA. There, a single station attests of that uplift, but the additional support from the long-term estimates from uplifted sequences of marine terraces [e.g., *Fairbridge and Hillaire-Marcel*, 1977] more robustly confirms the fast post glacial rebound of the area.

Along the West coast, Alaska is exposed to several major effects including strong tectonic activity, melting of the glaciers and the GIA. Among these three main contributions, while GIA and melting of the glaciers might explain the overall coastal uplift, fast tectonic activity is the most probable cause for the very sharp gradients in sea level rates associated with records with a reasonably small uncertainty. As an example, the only subsiding data displayed in this region in Figure 13 corresponds to the Cordova tide gauge, exhibiting a $\sim$ 20 years long rise in sea level following the 1964 Alaskan earthquake. Immediately at the southeast, the rate associated with the Juneau tide gauge is displayed as a blue circle on Figure 13 because it lies out of the reconstructed surface. This is only due to the fact that our reconstruction excludes such high

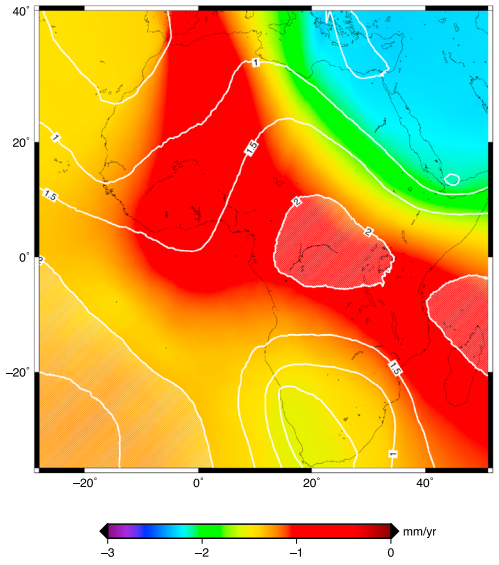


**Figure 18.** Same as Figure 14 for Africa.

absolute values for the rate of sea level variation. Otherwise, the reconstructed surface would exhibit even stronger gradients. When exiting this region adjacent to the Queen Charlotte-Fairweather fault, the surface is much smoother: Further south, from British Columbia to the north of California, relative sea level change is moderate (rates range from $0.2 \pm 0.5$ to $-0.9 \pm 1.5$ mm/yr), a value that increases southward to $1.5 \pm 0.4$ mm/yr in California. The standard deviation dramatically increases in Mexico and renders unrealistic to interpret our model, though subsidence is measured in most stations. Note that in this region, the probability density function is often strongly bimodal. In the United States coastline of the Gulf of Mexico, subsidence increases to abundantly reported fast subsidence rates, in Texas (for instance, Galveston subsides at −5.9 mm/yr due to groundwater mining, cf. *Rhein et al.* [2013]) and above in Louisiana where flooding recurrently threatens the entire coastline around the mouth of the Mississippi (critically exemplified by the ravaging effects of 2005 hurricane Katrina). Our model allows to bracket the estimates of sea level rise at the wavelength of the delta to $7 \pm 1.5$ mm/yr in the area. Such rates are caused by long-term, natural processes (normal faulting and compaction of recent sediments [e.g., *Meckel et al.*, 2007]) that are reenforced by harsh human action (water and hydrocarbon extraction and river drainage).

### 4.3. Australia

Australia has a fair number of tide gauges, the spatial density and quality (record length and uncertainty) of which mostly improves to the southeast (Figures 15 and 16). Overall, the resolution is fairly good, but the heterogeneous distribution jeopardizes the interpolation. Voronoi cells are few on average (~7) and rather large (Table 2). Our model reflects this distribution fairly well and features values for the standard deviation that precisely mirror this trend. Only along the eastern coast is relative sea level change well constrained, at a subsiding rate of $\sim 0.8 \pm 0.5$ mm/yr (within 95% confidence) to the north of Sidney, a value that increases to $\sim 1.5 \pm 0.7$ mm/yr closer to Brisbane (Figure 15). Elsewhere the model is rather uncertain except in Perth, that bears a pair of stations of remarkable quality. Whether or not they reveal local processes, they dominate the signal and compact the confidence interval to less than 1 mm/yr (Figure 15). At the continent scale, Australia seems to bend toward the north, where the fastest subsidence is inferred. However, given the uncertainties and standard deviation of our model prediction, it remains difficult to conclude on the processes at play without the caveat of overinterpreting the signal.

### 4.4. Africa

Besides South Africa, the record lengths of tide gauges in Africa are very short for the most part, which yields a poor resolution (Table 2). The data coverage is rather poor too, with less than 30 stations on the coasts of the entire continent, among which many cluster in South Africa, which causes large mean areas of the Voronoi cells, and few of them. This makes the uncertainties very large (often higher than 5 mm/yr, Figure 17). Note however that the surface reconstruction also benefits from constraints provided by tide gauges located on the Northern shores of the Mediterranean and on Mediterranean islands, as well as Atlantic islands, such as the Canary Islands (cf., e.g., the Santa Cruz de Tenerife with a record length $n_{20} = 56$). Thus, while South Africa is associated with the lowest values of the confidence interval (Figure 17) and standard deviation (Figure 18), the north of Africa is also characterized by relatively modest values. Elsewhere, the surface is reconstructed at a lower resolution compared to Europe and North America. Here the transdimensional Bayesian scheme has adapted to the level of information present in the data, and only provides a long wavelength description of the sea level rate. The posterior solution is described by an ensemble of models defined by a small number of large Voronoi cells describing regional averages. The average number of cells in the ensemble is 5.11 (compared to 31.2 for North America, for example, see Table 2). As in any

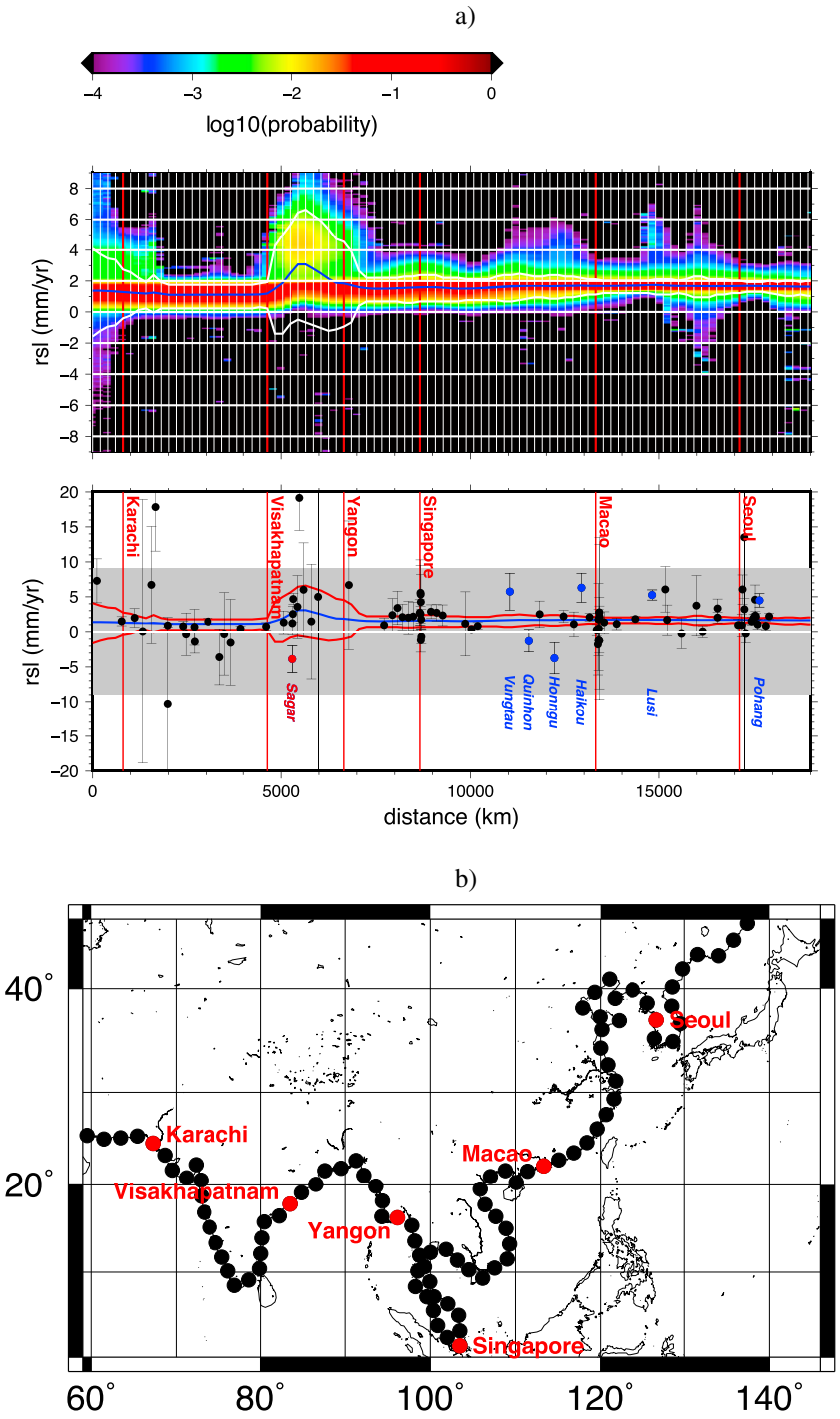


**Figure 19.** Same as Figure 12 for the coasts of Asia.

data inference problem, the level of uncertainty in the estimated surface trades-off with the level of resolution. Here this results in a relatively small confidence interval for the surface (1.9 mm/yr in average along the coasts, cf. Figure 17) typically smaller than the uncertainties associated with tide gauge data (average along the coasts: 11.1 mm/yr for all tide gauges and 2.7 mm/yr if tide gauges with uncertainties larger than 10 mm/yr are excluded, cf. Figure 17). This may seem paradoxical and counterintuitive, as surface errors for Africa (Figures 17 and 18) are often lower than for better resolved regions such as Europe (Figures 8d and 12) or North America (Figures 14 and 13). Furthermore, sensitivity tests as described in Appendix B

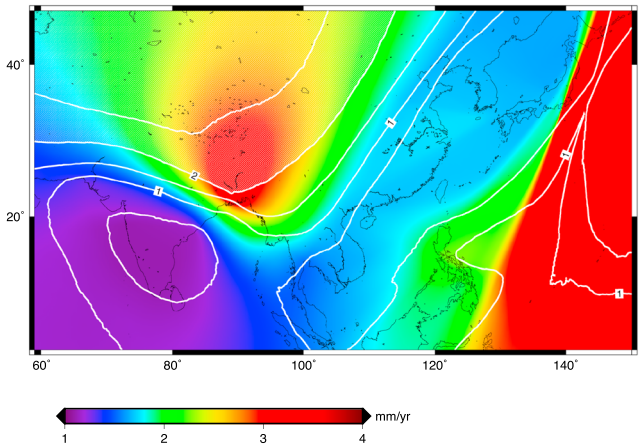


**Figure 20.** Same as Figure 14 for Asia.

indicate that excluding stations with short record length from the initial data set does not alter considerably the reconstructed surface (unless more than 90% of the tide gauges are rejected), thus casting doubt on its reliability. This is because estimated errors for Africa refer to the long wavelength information, whereas errors for Europe or North America refer to smaller scales, and hence might be larger. Thus, one should not directly compare error maps between different regions, but instead view these maps as a way to depict the reliability of the surface within a given region.

Overall, for the wavelength resolved in this region, our modeling proves worthwhile in South Africa, as we can confidently assert that sea level drops at $\sim 1.5 \pm 0.5$ mm/yr with a 95% confidence. The causes of that relative coastal uplift are unclear as few direct measurements of vertical ground motion are available. It could be tempting to relate this uplift to the long-term uplift of South Africa above the convecting mantle, but the large magnitude most likely corresponds again to the GIA.

### 4.5. Asia

Many tide gauges in Asia have a long record length, often in excess of 30 years and up to 80 years, making the local uncertainties rather small. The density of the stations is rather high (yet not as high as Europe), and the many coastlines facilitate their two-dimensional interpolation. Consequently, values for the standard deviation are typically lower than 1 mm/yr (Figure 19). Overall, the coasts of continental Asia, from Pakistan to Vladivostok, are subsiding. In Pakistan and India, sea level rises at $\sim 0.8 \pm 1$ mm/yr within a 95% confidence interval (Figures 20 and 19). Along the coasts of continental SE Asia, from Burma to Russia, subsidence increases to $\sim 1.5 \pm 0.5$ mm/yr within a 95% confidence interval. Overall the signal is extremely smooth along the coast. Only in Bangladesh does the model become more blurry. Nevertheless, the results are worthwhile, as they bracket the long wavelength subsidence rates in the Ganges-Brahmaputra delta to $\sim 2.5 \pm 3$ mm/yr; this value shall not be mixed with the local subsidence that reaches extremely high values (up to $20 \pm 5$ mm/yr). The tide gauge of Sagar appears as an outlier as it is indicative of a $4 \pm 2$ mm/yr relative uplift, thus with a rather high degree of confidence. In a first attempt, Sagar was found to bias the interpolation in this dominantly subsiding area, lowering the mean value and increasing the standard deviation. It has been removed from the surface reconstruction whose results are presented here.

We emphasized above the high quality of the signal, given that the standard deviation tends to very low values and that the uncertainties are low. However, it is noteworthy that several stations with a low variance depart from our model (blue circles, Figure 19); both anomalous uplifts and subsidences are obtained, some of these already pointed in earlier studies (see, for example, *Han and Huang* [2008], in the case of the Lusi tide gauge). Multiple local causes may be responsible for these features: the station of Quin Hon is uplifting at a fast rate, together with the neighboring Honngu station. Both are located along the extremely active Red River—Ailao Shan fault system, that may cause fast uplift. Indeed, the large sequence of marine terraces in the vicinity of Honngu attest for a continuous uplift throughout the Quaternary [see *Pedoja et al.*, 2011, 2014, and references therein]. Conversely, the fast subsidence of the Vung Tau tide gauge clearly outlines the effect of the Mekong river delta although its relocation during the twentieth century may also contribute to the anomalous record. Another striking feature is the Japan dichotomy, where the eastern, Pacific, coasts of Honshu, and Hokkaido subside up to 3 times faster than their western counterpart... This situation could be tentatively explained by vertical ground motion above the subduction zone, that shows an eastward tilt of the northern islands. Yet the coseismic vertical displacement linked to the 2011 Tohoku earthquake [*Grapenthin and Freymueller*, 2011] did not counteract that possibly interseismic tendency. In addition, a specific surface reconstruction dedicated to Japan (a much smaller region with a relatively good tide gauge record) presents specific local features that do not appear on the global map shown here (Figure 20).

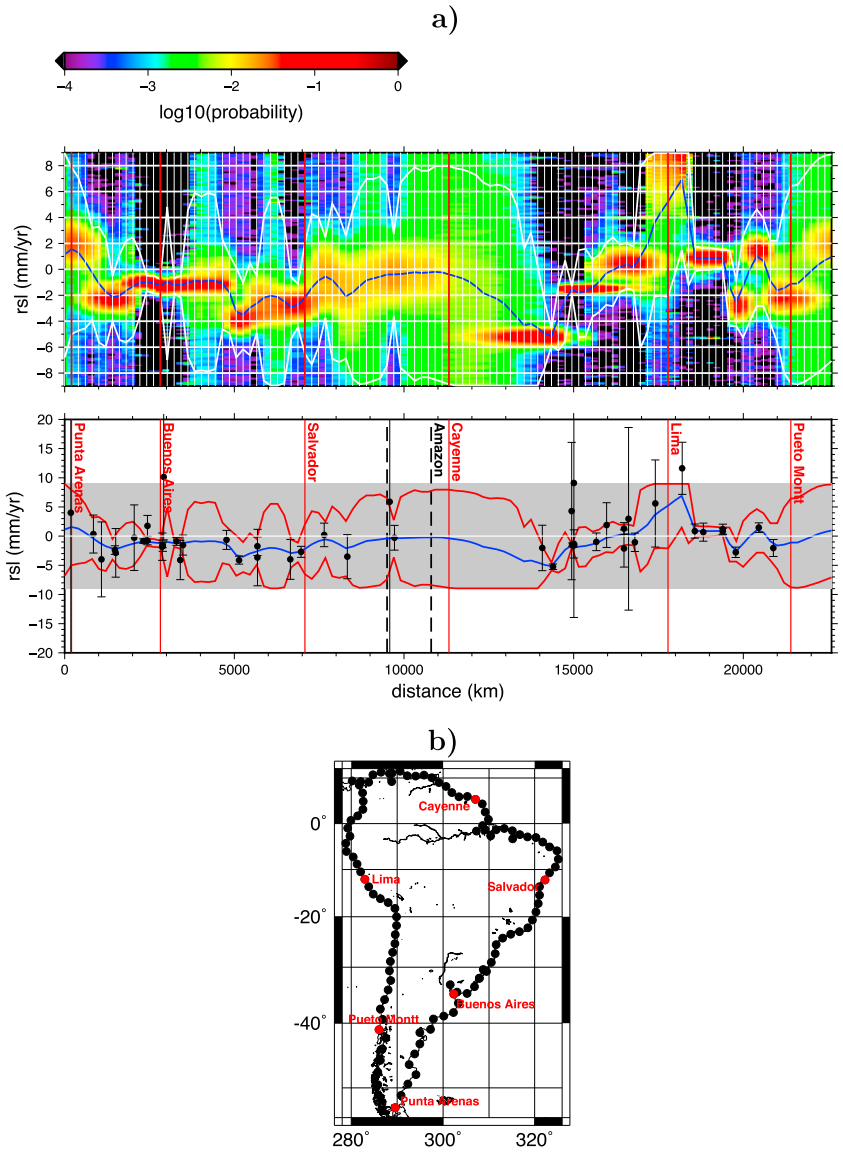


**Figure 21.** Same as Figure 12 for the coasts of South America.

Such departures from the longer-scale surface are similar to the ones presented as blue circles in Figure 19. While the tide gauge record is much longer than in the African case, the average number of Voronoi cells for Asia is comparable (see Table 2). Due to the overall smoothness of the rate of sea level rise obtained at most tide gauge records, the typical wavelength resolved by the surface reconstruction is thus relatively large in spite of the large number of stations in the region. As a result, features at much shorter wavelengths are interpreted by our method as anomalous signals. The southeastern coast of Asia is particularly threatened in terms of economic losses caused by sea level rise *Hallegatte et al.* [2013]; a probabilistic assessment of the threat is thus of prime importance.

### 4.6. South America

In South America (Figures 21 and 22), the record lengths are not uniform: while several stations in Chile and Argentina have more than 40 years of record, the Andean states (from Venezuela to Peru) and Brazil have a poorer record. However, the spatial distribution of the stations is rather even (as opposed to Africa for instance). Overall, the characteristics of the tide gauge record (high uncertainty, approximately even distribution) induces a dominantly high standard deviation (Figure 22) together with a high mean number of Voronoi cells (see Table 2) which could in principle be expected to reflect the spatial precision of the result;

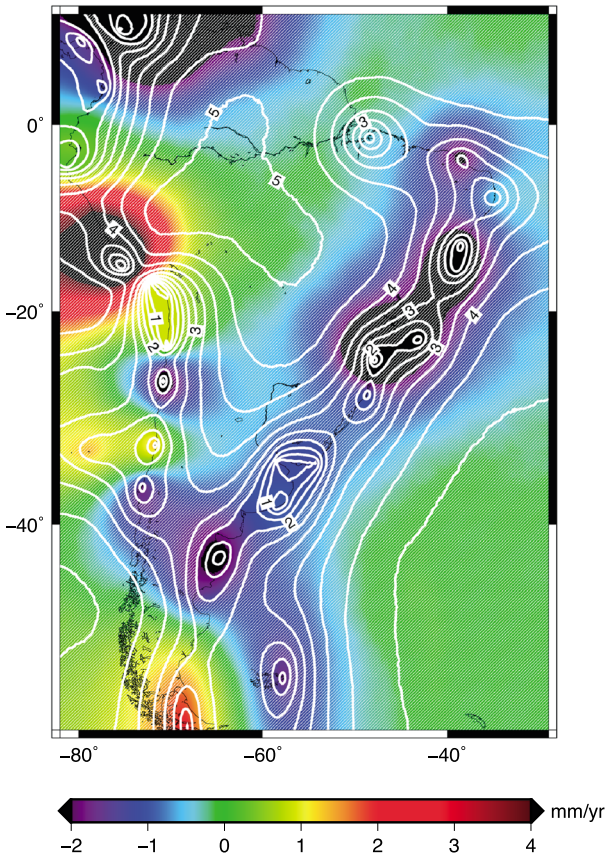


**Figure 22.** Same as Figure 14 for South America.

in fact, this results from the roughness of the signal that cannot be resolved with a small amount of cells but that, as a consequence, raises the standard deviation to higher values than the local uncertainties. This is further illustrated by the sensitivity tests performed for the uncertainty (cf. Appendix B): discarding tide gauges with short record length such as San Juan in Peru ($n_{20} = 9$ years), immediately alters the surface locally. This specificity of South America is further discussed below (section 5).

Our interpolation nevertheless depicts the trend of relative sea level change, though the standard deviation prevents from assigning precise numbers to the magnitudes. Along the Atlantic coast of South America, the coast is uplifting from Brazil to Patagonia. Interestingly, our model suggests that Patagonia is subsiding at a fast rate, at odds with the known effects of the GIA [e.g., *Peltier*, 1998] or dynamic topography [*Guillaume et al.*, 2009] that conversely indicates that those mechanism are jointly uplifting Patagonia at a faster rate than the rest of South America. Two stations in the region of the Straight of Magallanes (Punta Arenas, Caleta Percy) are indeed associated with large values of subsidence, but their uncertainty is so large that the reason for this regional trend rather has to be associated with a station located further South, Ushuaia, also recording subsidence, but with a much smaller uncertainty (2.58 ± 0.67 mm/yr)—since it is relatively distant from the coast line considered here, it does not appear on Figure 21 but is the main contributor to the reconstructed surface in this region. This subsidence effect in Patagonia shall thus be interpreted as resulting from local faulting in this tectonically active area. Similarly, fast subsidence is locally measured at one station in the Buenos Aires area (Isla Martin Garcia), at odds with other nearby records that cluster toward moderate uplift. This is most certainly a response to the longterm sediment loading on the Rio de la Plata [e.g., *Pedoja et al.*, 2010] where this station is precisely located. The uncertainty associated with this station is large enough not to alter the interpolation in an area where many stations conversely are reliable.

## 5. Conclusion

We present a new surface reconstruction procedure for the average rate of relative sea level variation during the twentieth century: average rates are computed from the tide gauges record so that only islands and coastal regions are concerned. Furthermore, we focus here on relative sea level including the VLM signal so that climatic effects, predominant for absolute sea level, appear here as secondary contributions, often hidden in the typical uncertainty inherent to our method. As the models based on a Voronoi tessellation adapt to the level of information in the various regions considered here, the Bayesian inference method proves well suited to the strong heterogeneity of tide gauges distribution as well as of the large variations of their record length. Sensitivity tests performed on tide gauges' record length demonstrate that the reconstructed surfaces are not contaminated by stations with short record lengths, unless the spatial resolution is extremely poor. A significant benefit of this approach is that no data selection is required a priori: the very few outliers encountered in our study (three in total out of 1310 tide gauges) are instantly distinguishable in the reconstructed surface; other anomalous stations naturally lie out of the confidence interval and

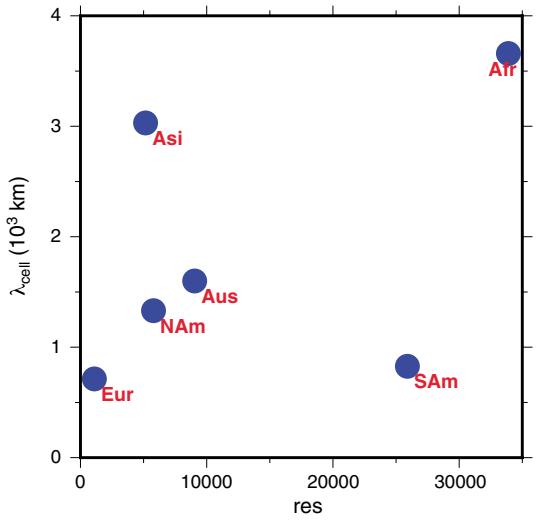


**Figure 23.** Typical length scale of Voronoi cells $\lambda_{cell}$ as a function of res, the "resolution of the model" computed as the area of a given region divided by $n_{20}^{cum}$, i.e., the sum of the record lengths of all tide gauges involved in the surface reconstruction (data are presented in Table 2).

can be analyzed subsequently. In addition, each point of the reconstructed surface is defined through a probability density function, a format particularly well adapted for this specific datum: although this aspect slightly complicates the appraisal of the solution, since several estimates (e.g., average, median, maximum, and standard deviation) can be proposed, the societal impact of sea level rise renders useful the expression of sea level variation in terms of probability, as is the case for other climate-related variables in the framework of IPCC reports.

One major characteristic of the reconstructed surfaces is that the spatial resolution strongly varies among the six large regions introduced and within a given region. A direct consequence is that sea level variations recorded at tide gauges associated with small uncertainties that depart from the regional trend can either cause a problematic distortion of the surface (this is the case for the three outliers Poti, Patrai, and Sagar reported on the coasts of the six considered regions) or simply lie out of the confidence interval without affecting much the reconstructed surface (this is the case of more numerous tide gauges reported as blue dots on the figures displaying PDFs along the coasts). The latter correspond to regions that are sufficiently well constrained to reject the influence of these anomalous data, while the former are associated with regions with poorer coverage. Although we did not investigate thoroughly the causes leading to a very localized departure from the surface for each anomalous station, several examples (such as Venezia) tend to indicate that anthropogenic effects are a likely explanation, while some others (such as Honngu or Patrai) are clearly caused by fast local tectonics. Other relatively small-scale geological effects have been shown to modify the reconstructed surface as long as the data density is sufficient (this is probably the case in Alaska, although other effects such as changes in ice coverage also contribute). In summary, local anthropogenic effects and faulting lead to anomalous records that depart from the reconstructed surface. Other effects associated with tectonic displacements, even if localized, are shown to deform the reconstructed surface if recorded by a large enough number of tide gauges.

Figure 23 further shows that the characteristic precision of the reconstructed surface, measured as the average area $A_{cell}$ (or characteristic length $\lambda_{cell} = \sqrt{A_{cell}}$) of Voronoi cells for a given region is a function of the "resolution" $res_A$ of the tide gauge data set in this region (measured as its area divided by the cumulated number of years associated with all tide gauge records used in the surface reconstruction, $n_{20}^{cum}$) for four of the six regions considered in the present study. Europe is associated with the best "resolution" (smallest value of $res_A$) and correspondingly, to the smallest typical length scale of Voronoi cells. From this reference, results for North America, Australia, and Africa display a unique global trend with increasing values of $res_A$ (less and less well resolved) and increasing typical length scales associated with the reconstructed surface. In the case of North America, the decrease in resolution is clearly heterogeneous, with areas such as the Atlantic coasts possibly as precisely reconstructed as their European counterparts, while other areas such as Mexico and Central America are poorly resolved. Australia is even less well resolved especially in the northern regions of the continent. Africa constitutes an end-member in our study, with very poor resolution and, consequently, a large length scale typical of the model's precision. Again, since the data distribution within this region is heterogeneous, the typical length scale $\lambda_{cell}$ shall not be confused with a uniform characteristic length scale above which the reconstructed surface is reliable: although it would be tempting to associate long wavelength features of the reconstructed surface to phenomena involving spatial scales of several thousands of kilometers such as the dynamic topography associated with the African superswell

[cf., e.g., *Lithgow-Bertelloni and Silver*, 1998], it is not clear whether the lack of stations in the western coasts of Africa authorizes such a conclusion.

Asia and South America clearly deviate from the trend discussed above (cf. Figure 23). The fact that the average length scale of Voronoi cells $\lambda_{cell}$ in the case of Asia is approximately as large as for Africa, in spite of a quite dense and relatively homogeneous tide gauge record with relatively small uncertainties indicates that the smoothness of the reconstructed surface is not an artifact. In spite of departures from this smooth solution (cf. blue symbols in Figure 19) and sharp gradients as is the case for Japan (Figure 20), at wavelengths corresponding to several thousands of kilometers, sea level rise is relatively uniform on the coasts of Asia, except in the region corresponding to the Ganges-Brahmaputra delta. Conversely, the case of South-America is puzzling since, in spite of a globally poor coverage by tide gauges, the average number of Voronoi cells is comparable to the one obtained for Europe. We interpret this last result as a consequence of the intrinsic roughness of the surface, revealed by a relatively homogeneous distribution of tide gauges (even if these are associated with moderately long record lengths).

Given this heterogeneity in resolution, the main robust characteristics of the reconstructed surfaces include the following:

1. The high precision obtained in Europe with the pronounced uplift of the Fennoscandian region (whose edges are associated with sharp gradients), as the most prominent feature in the reconstructed surface;
2. The heterogeneous precision of North America: while the West and East coasts of the United States are approximately as well resolved as their European counterparts in the Atlantic (although the North American coasts of the Atlantic present significantly stronger rates of sea level rise), coasts in Central America are not well resolved;
3. Although the tide gauge record in Asia would allow the description of gradients in relative sea level change at an intermediate wavelength of a few thousand kilometers, a relatively flat surface is obtained except for the subsiding Ganges-Brahmaputra delta; although specific records depart from the confidence interval locally (either because of fast tectonics or of anthropogenic effects), a reliable conclusion is the globally uniform rise in sea level along the Asian coasts.

As already indicated, average rates for the twentieth century ($r_{20}$) often correspond to time series at tide gauges that record the most recent variations of relative sea level rise. The recent era of higher than average sea level rise since 1990, also witnessed by satellite altimetry, thus contribute to the reconstructed surface with a relatively larger weight when compared to variations in sea level for the period 1900–1950, recorded by only few sites. As a result, the reconstructed surfaces can be considered as a high estimate of the actual time average for the twentieth century. Regions covered by only recent tide gauges, in addition to displaying larger uncertainties, might also be affected by this bias. In regions with a correct coverage, however, we notice that all tide gauges with a long record (and thus a small uncertainty) all provide rates that lie in the confidence interval reported for the reconstructed surface. In addition, we show (cf. Figure 5) that rates computed for the 1900–present period, used to compute the reconstructed surfaces, compare well to rates computed for the 1900–1961 period (the latter associated to larger uncertainties).

Finally, relative sea level rise measured by tide gauges, although ultimately the most significant measurement in terms of societal implications, is dominated by contributions from the GIA [cf., e.g., *Peltier*, 1998] or other solid Earth effects identified at some locations [*Wöppelmann et al.*, 2009]. Taking advantage of recent GPS evaluation of VLM [*Wöppelmann et al.*, 2009] and assuming that such records, since the 1990s, are representative of the whole twentieth century (except for well-documented fast tectonics events, timescales for the vertical displacement of the solid Earth are longer), it will be possible with our tool to compute similar reconstructed surfaces for absolute sea level variations indicative of climatic forcing. This will be the topic of a forthcoming study.

## Appendix A: Estimating the Rate of Sea Level Rise From TGs

We have considered two families of curve to fit the TG annual data sets since year 1900. First, a linear fit is proposed that follows almost identically the procedure proposed by *Spada and Galassi* [2012]. Let $(x_i, y_i)_{i=1,n}$ denote the annual RLR PSMSL data at a given TG, for a given period. The number of valid records is $n$ ($n = n_{20}$

for the period 1900–present, $n = n_I$ for the period 1900–1961, $n = n_{II}$ for the period 1970–present). The least squares rate of sea level variation is then

$$r = \frac{nS_{xy} - S_x S_y}{nS_{xx} - S_x^2} \tag{A1}$$

where

$$\begin{cases} S_{xy} = \sum_{i=1}^{n} x_i y_i \\ S_x = \sum_{i=1}^{n} x_i \\ S_y = \sum_{i=1}^{n} y_i \\ S_{xx} = \sum_{i=1}^{n} x_i^2 \end{cases} \tag{A2}$$

We also propose a fit by a second-degree curve, i.e., the function $y = ax^2 + bx + c$ leading to the least squares parabola. The quadratic coefficient $a$ is then

$$a = \frac{(nS_{xx} - S_x^2)(nS_{xxy} - S_{xx}S_y) - (nS_{xxx} - S_{xx}S_x)(nS_{xy} - S_x S_y)}{(nS_{xx} - S_x^2)(nS_{xxxx} - S_{xx}^2) - (nS_{xxx} - S_x S_{xx})^2} \tag{A3}$$

where the additional following sums have been introduced

$$\begin{cases} S_{xxy} = \sum_{i=1}^{n} x_i^2 y_i \\ S_{xxx} = \sum_{i=1}^{n} x_i^3 \\ S_{xxxx} = \sum_{i=1}^{n} x_i^4 \end{cases} \tag{A4}$$

Note that acceleration of the sea level variation is $2a$. Coefficients $b$ and $c$ can then be obtained for example from

$$b = \left(nS_{xy} - S_x S_y - a(nS_{xxx} - S_x S_{xx})\right) / \left(nS_{xx} - S_x^2\right) \tag{A5}$$

and

$$c = \left(S_y - aS_{xx} - bS_x\right) / n \tag{A6}$$

respectively.

In order to compute the uncertainty $\sigma$ on these estimates, we follow again the procedure introduced by *Spada and Galassi* [2012] (equations (2) and (3) in their article) with a 95% confidence interval based on the appropriate Student's $t$ distribution.

## Appendix B: Sensitivity Tests for the Uncertainty

As indicated in the text, the estimated error on the $i$th tide gauge $e_i$ is proportional to the relative, formal, uncertainty derived from the least squares fit (see section 2.2 and Appendix A), $\sigma_i$:

$$e_i = \lambda \sigma_i \tag{B1}$$

where $\lambda$ is an unknown scaling factor, constrained in the reconstruction procedure. As an example, $\lambda \simeq 2.3$ for the reconstructed surface in Europe, a value comparable to the estimation error reported by *Church and White* [2011] indicating that, due to autocorrelation, "the number of effective degrees of freedom is only a quarter of the number of years of data," thus leading approximately to a twofold increase of our formal uncertainty $\sigma_i$.

Qualitatively, this formula associates the largest uncertainties to tide gauges with short record length (yearly to decadal oscillations deteriorate the quality of the fit for such stations). Since climatic variations might also bias the evaluation of sea level variation as larger amplitude, variations, occurring over several years to several decades, could be interpreted as representative of the whole century in the case of relatively short record lengths; we nevertheless produced a sensitivity study by

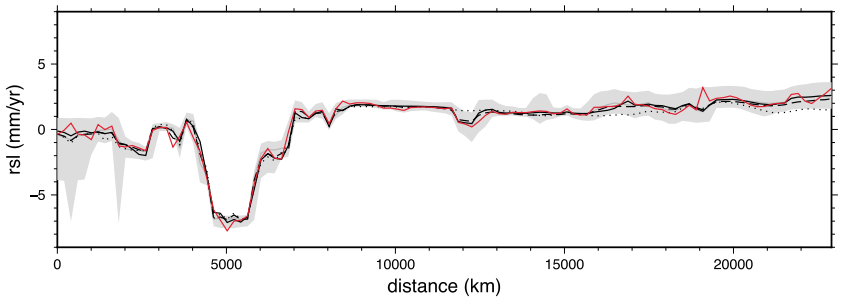


**Figure B1.** Sensitivity test for tide gauge record length—the case of Europe. The standard surface reconstruction including all tide gauges is displayed in grey (the solid grey curve displays the average at a given location on the coast and the lighter grey envelope displays the 95% interval. All other curves display averages obtained for the various tests. Tests where recent tide gauges have been excluded are in black: only stations with at least 10 years of record length (solid curve), with at least 20 years (dashed curve), and with at least 40 years (dotted curve). The red curve displays results obtained using equation (B2) for the estimation of the data noise $e_i$.

1. excluding stations with record lengths $n_{20}$ shorter than 10 years, 20 years, 40 years and
2. proposing a different formula for the uncertainty:

$$e_i = \lambda' \left(\sigma_i / n_{20,i}\right) \tag{B2}$$

Note that equation (B2) further disqualifies stations with short record lengths: the final uncertainty $e_i$ of a station with $n_{20} = 10$, already associated to a formal relative uncertainty $\sigma_i$ typically 10 times larger than a station with $n_{20} = 100$ (see Figure 5), will ultimately be 100 times larger.

These tests indicate that tide gauges with short record lengths do not affect the reconstructed surface: Figure B1 displays the results in the case of Europe. Reconstructed surfaces excluding tide gauges with $n_{20} = 10$ years or 20 years only depart very little from the reference case ($\simeq$ 0.1–0.2 mm/yr in average with a maximum local difference of $\simeq$ 1 mm/yr). Note that the use of equation (B2) to evaluate $e_i$, strongly penalizing stations with small values of $n_{20}$ induce more roughness of the reconstructed surface for Europe (this remains true for all other regions, not shown here). Only in the case of a very poor data set (namely, for Africa and South America) does the rejection of tide gauges with $n_{20} < 40$ years (i.e., 92% of tide gauges for Africa) alter significantly the reconstructed surface even though the latter is already smooth in the reference case, due to a lack of resolution. See also the text dedicated to each region for further details.

**Acknowledgments**
All the data presented in this article are available upon request to the corresponding author. This work benefited from the ANR grant GiSeLe and from the Miller institute for basic research in science, at the University of California, Berkeley.

## References

Ablain, M., A. Cazenave, G. Valladeau, and S. Guinehut (2009), A new assessment of the error budget of global mean sea level rate estimated by satellite altimetry over 1993–2008, *Ocean Sci.*, *5*, 193–201.

Bayes, T. (1763), *An Essay Towards Solving a Problem in the Doctrine of Chances*, C. Davis, Printer to the Royal Society of London, London, U. K.

Bodin, T., M. Salmon, B. Kennett, and M. Sambridge (2012a), Probabilistic surface reconstruction from multiple data sets: An example for the Australian moho, *J. Geophys. Res.*, *117*, B10307, doi:10.1029/2012JB009547.

Bodin, T., M. Sambridge, N. Rawlinson, and P. Arroucau (2012b), Transdimensional tomography with unknown data noise, *Geophys. J. Int.*, *189*, 1536–1556.

Broerse, D. B. T., L. L. A. Vermeersen, R. E. M. Riva, and W. van der Wal (2011), Ocean contribution to co-seismic crustal deformation and geoid anomalies: Application to the 2004 December 26 Sumatra-Andaman earthquake, *Earth Planet. Sci. Lett.*, *305*, 341–349, doi:10.1016/j.epsl.2011.03.011.

Calafat, F. M., D. P. Chambers, and M. N. Tsimplis (2014), On the ability of global sea level reconstructions to determine trends and variability, *J. Geophys. Res. Oceans*, *119*, 1572–1592, doi:10.1002/2013JC009298.

Cazenave, A., and W. Llovel (2010), Contemporary sea level rise, *Annu. Rev. Mar. Sci.*, *2*, 145–173, doi:10.1146/annurev-marine-120308-081105.

Cazenave, A., and R. S. Nerem (2004), Present-day sea level change: Observations and causes, *Rev. Geophys.*, *42*, RG3001, doi:10.1029/2003RG000139.

Cazenave, A., and F. Remy (2011), Sea level change and climate: Measurements and causes of changes, *Wiley Interdiscip. Rev. Clim. Change*, *2*, 647–662.

Christiansen, B., T. Schmith, and P. Thejll (2010), A surrogate ensemble study of sea level reconstructions, *J. Clim.*, *23*, 4306–4326, doi:10.1175/2010JCLI3014.1.

Chronis, G., D. J. Piper, and C. Anagnostou (1991), Late quaternary evolution of the gulf of Patras, Greece: Tectonism, deltaic sedimentation and sea-level change, *Mar. Geod.*, *97*(1–2), 191–209, doi:10.1016/0025-3227(91)90026-Z.

Church, J., et al. (2013), Sea level change, in *Climate Change 2013: The Physical Science Basis. Contribution of Working Group I to the Fifth Assessment Report of the Intergovernmental Panel on Climate Change*, edited by T. Stocker et al., pp. 1137–1216, Cambridge Univ. Press, Cambridge, U. K., and New York.

Church, J. A., and N. J. White (2006), A 20th century acceleration in global sea-level rise, *Geophys. Res. Lett.*, *33*, L01602, doi:10.1029/2005GL024826.

Church, J. A., and N. J. White (2011), Sea-level rise from the late 19th to the early 21st century, *Surv. Geophys.*, *32*, 585–602, doi:10.1007/s10712-011-9119-1.

Church, J. A., N. J. White, R. Coleman, K. Lambeck, and J. X. Mitrovica (2004), Estimates of the regional distribution of sea level rise over the 1950–2000 period, *J. Clim.*, *17*, 2609–2625.

Conrad, C. P. (2013), The solid Earth's influence on sea level, *Geol. Soc. Am. Bull.*, *125*, 1027–1052, doi:10.1130/B30764.1.

Conrad, C. P., and B. H. Hager (1997), Spatial variations in the rate of sea level rise caused by the present-day melting of glaciers and ice sheets, *Geophys. Res. Lett.*, *24*, 1503–1506, doi:10.1029/97GL01338.

de Klerk, P., A. Haberl, A. Kaffke, M. Krebs, I. Matchutadze, M. Minke, J. Schulz, and H. Joosten (2009), Vegetation history and environmental development since ca 6000 cal yr BP in and around Ispani 2 (Kolkheti lowlands, Georgia), *Quat. Sci. Rev.*, *28*(9–10), 890–910, doi:10.1016/j.quascirev.2008.12.005.

Dettmer, J., S. Dosso, and C. Holland (2010), Trans-dimensional geoacoustic inversion, *J. Acoust. Soc. Am.*, *128*, 3393–3405.

Dettmer, J., S. Molnar, G. Steininger, S. E. Dosso, and J. F. Cassidy (2012), Trans-dimensional inversion of microtremor array dispersion data with hierarchical autoregressive error models, *Geophys. J. Int.*, *188*, 719–734, doi:10.1111/j.1365-246X.2011.05302.x.

Douglas, B. C. (1991), Global sea level rise, *J. Geophys. Res.*, *96*, 6981–6992, doi:10.1029/91JC00064.

Fairbridge, R. W., and C. Hillaire-Marcel (1977), An 8,000-yr palaeoclimatic record of the 'Double-Hale' 45-yr solar cycle, *Nature*, *268*, 413–416, doi:10.1038/268413a0.

Farrell, W. E., and J. A. Clark (1976), On postglacial sea level, *Geophys. J. R. Astron. Soc.*, *46*, 647–667, doi:10.1111/j.1365-246X.1976.tb01252.x.

Ferentinos, G., M. Brooks, and T. Doutsos (1985), Quaternary tectonics in the gulf of Patras, Western Greece, *J. Struct. Geol.*, *7*(6), 713–717, doi:10.1016/0191-8141(85)90146-4.

García, D., I. Vigo, B. F. Chao, and M. C. Martínez (2007), Vertical crustal motion along the mediterranean and black sea coast derived from ocean altimetry and tide gauge data, *Pure Appl. Geophys.*, *164*, 851–863, doi:10.1007/s00024-007-0193-8.

Geyer, C., and J. Møller (1994), Simulation procedures and likelihood inference for spatial point processes, *Scand. J. Stat.*, *21*(4), 359–373.

Grapenthin, R., and J. T. Freymueller (2011), The dynamics of a seismic wave field: Animation and analysis of kinematic GPS data recorded during the 2011 Tohoku-Oki earthquake, Japan, *Geophys. Res. Lett.*, *38*, L18308, doi:10.1029/2011GL048405.

Green, P. (1995), Reversible jump MCMC computation and Bayesian model selection, *Biometrika*, *82*, 711–732.

Green, P. (2003), Trans-dimensional Markov chain Monte Carlo, in *Highly Structured Stochastic Systems*, vol. 27, edited by P. J. Green, N. L. Hjord, and S. Richardson, pp. 179–198, Oxford Univ. Press, Oxford, U. K.

Guillaume, B., J. Martinod, L. Husson, M. Roddaz, and R. Riquelme (2009), Neogene uplift of central eastern Patagonia: Dynamic response to active spreading ridge subduction?, *Tectonics*, *28*, TC2009, doi:10.1029/2008TC002324.

Guillaume, B., L. Husson, F. Funiciello, and C. Faccenna (2013), The dynamics of laterally variable subductions: Laboratory models applied to the Hellenides, *Solid Earth*, *4*(2), 179–200, doi:10.5194/se-4-179-2013.

Hallegatte, S., C. Green, R. J. Nicholls, and J. Corfee-Morlot (2013), Future flood losses in major coastal cities, *Nat. Clim. Change*, *3*, 802–806, doi:10.1038/nclimate1979.

Hamlington, B. D., R. R. Leben, R. S. Nerem, W. Han, and K.-Y. Kim (2011), Reconstructing sea level using cyclostationary empirical orthogonal functions, *J. Geophys. Res.*, *116*, C12015, doi:10.1029/2011JC007529.

Han, G., and W. Huang (2008), Pacific decadal oscillation and sea level variability in the Bohai, Yellow, and East China Seas, *J. Phys. Oceanogr.*, *38*, 2772–2783.

Haq, B., and S. Schutter (2008), A chronology of Paleozoic sea-level changes, *Science*, *322*, 64–68.

Hastings, W. (1970), Monte Carlo simulation methods using Markov chains and their applications, *Biometrika*, *57*, 97–109.

Holgate, S. J., and P. L. Woodworth (2004), Evidence for enhanced coastal sea level rise during the 1990s, *Geophys. Res. Lett.*, *31*, L07305, doi:10.1029/2004GL019626.

Holgate, S. J., A. Matthews, P. L. Woodworth, L. J. Rickards, M. E. Tamisiea, E. Bradshaw, P. R. Foden, K. M. Gordon, S. Jevrejeva, and J. Pugh (2013), New data systems and products at the permanent service for mean sea level, *J. Coastal Res.*, *29*, 493–504, doi:10.2112/JCOASTRES-D-12-00175.1.

Houston, J., and R. Dean (2011), Sea-level acceleration based on U.S. tide gauges and extensions of previous global-gauge analyses, *J. Coastal Res.*, *27*, 409–417.

Iaffaldano, G., T. Bodin, and M. Sambridge (2012), Reconstructing plate-motion changes in the presence of finite-rotations noise, *Nat. Commun.*, *3*, 1048.

Iaffaldano, G., T. Bodin, and M. Sambridge (2013), Slow-downs and speed-ups of India–Eurasia convergence since: Data-noise, uncertainties and dynamic implications, *Earth Planet. Sci. Lett.*, *367*, 146–156.

Intergovernmental Panel on Climate Change (2013), Summary for policymakers, in *Climate Change 2013: The Physical Science Basis. Contribution of Working Group I to the Fifth Assessment Report of the Intergovernmental Panel on Climate Change*, edited by T. Stocker et al., pp. 3–29, Cambridge Univ. Press, Cambridge, U. K., and New York.

Jevrejeva, S., A. Grinsted, J. C. Moore, and S. Holgate (2006), Nonlinear trends and multiyear cycles in sea level records, *J. Geophys. Res.*, *111*, C09012, doi:10.1029/2005JC003229.

Kemp, A. C., B. P. Horton, J. P. Donnelly, M. E. Mann, M. Vermeer, and S. Rahmstorf (2011), Climate related sea-level variations over the past two millennia, *PNAS*, *108*, 11,017–11,022, doi:10.1073/pnas.1015619108.

Kereselidze, D., K. Bilashvili, V. Trapaidze, and G. Bregvadze (2011), Hydrological regime of load discharge of the rivers of Kolkhetu Lowland, Georgia, paper presented at 11th International Multidisciplinary Scientific GeoConference (SGEM 2011), vol. 2, pp. 853–858.

Lithgow-Bertelloni, C., and P. G. Silver (1998), Dynamic topography, plate driving forces and the African superswell, *Nature*, *395*, 269–272, doi:10.1038/26212.

Long, A. J., N. L. M. Barlow, W. R. Gehrels, M. H. Saher, P. L. Woodworth, R. G. Scaife, M. J. Brain, and N. Cahill (2014), Contrasting records of sea-level change in the eastern and western North Atlantic during the last 300 years, *Earth Planet. Sci. Lett.*, *388*, 110–122, doi:10.1016/j.epsl.2013.11.012.

Malinverno, A. (2002), Parsimonious Bayesian Markov chain Monte Carlo inversion in a nonlinear geophysical problem, *Geophys. J. Int.*, *151*(3), 675–688.

Malinverno, A., and V. A. Briggs (2004), Expanded uncertainty quantification in inverse problems: Hierarchical Bayes and empirical Bayes, *Geophysics*, *69*, 1005–1016, doi:10.1190/1.1778243.

Malinverno, A., and R. L. Parker (2006), Two ways to quantify uncertainty in geophysical inverse problems, *Geophysics*, *71*, W15–W27, doi:10.1190/1.2194516.

Meckel, T. A., U. S. Ten Brink, and S. J. Williams (2007), Sediment compaction rates and subsidence in deltaic plains: Numerical constraints and stratigraphic influences, *Basin Res.*, *19*(1), 19–31, doi:10.1111/j.1365-2117.2006.00310.x.

Metropolis, N., et al. (1953), Equations of state calculations by fast computational machine, *J. Chem. Phys.*, *21*(6), 1087–1091.

Meyssignac, B., M. Becker, W. Llovel, and A. Cazenave (2012), An assessment of two-dimensional past sea level reconstructions over 1950–2009 based on tide-gauge data and different input sea level grids, *Surv. Geophys.*, *33*, 945–972, doi:10.1007/s10712-011-9171-x.

Milne, G. A., and J. X. Mitrovica (1998), Postglacial sea-level change on a rotating Earth, *Geophys. J. Int.*, *133*, 1–19, doi:10.1046/j.1365-246X.1998.1331455.x.

Mitrovica, J. X., M. E. Tamisiea, J. L. Davis, and G. A. Milne (2001), Recent mass balance of polar ice sheets inferred from patterns of global sea-level change, *Nature*, *409*, 1026–1029.

Moucha, R., A. M. Forte, J. X. Mitrovica, D. B. Rowley, S. Quéré, N. A. Simmons, and S. P. Grand (2008), Dynamic topography and long-term sea-level variations: There is no such thing as a stable continental platform, *Earth Planet. Sci. Lett.*, *271*, 101–108, doi:10.1016/j.epsl.2008.03.056.

Nakiboglu, S., and K. Lambeck (1991), Secular sea level change, in *Glacial Isostasy, Sea-Level and Mantle Rheology*, edited by R. Sabadini, K. Lambeck, and E. Boschi, pp. 237–258, Kluwer Acad., Dordrecht, Netherlands.

Nerem, R., D. Chambers, C. Choe, and G. Mitchum (2010), Estimating mean sea level change from the topex and Jason altimeter missions, *Mar. Geod.*, *33*, 435–446.

Ostanciaux, É., L. Husson, G. Choblet, C. Robin, and K. Pedoja (2012), Present-day trends of vertical ground motion along the coast lines, *Earth Sci. Rev.*, *110*, 74–2, doi:10.1016/j.earscirev.2011.10.004.

Pedoja, K., V. Regard, L. Husson, J. Martinod, B. Guillaume, E. Fucks, M. Iglesias, and P. Weill (2010), Uplift of Quaternary shorelines in eastern Patagonia: Darwin revisited, *Geomorphology*, *127*, 121–142, doi:10.1016/j.geomorph.2010.08.003.

Pedoja, K., et al. (2011), Relative sea-level fall since the last interglacial stage: Are coasts uplifting worldwide?, *Earth Sci. Rev.*, *108*, 1–15, doi:10.1016/j.earscirev.2011.05.002.

Pedoja, K., et al. (2014), Coastal staircase sequences reflecting sea-level oscillations and tectonic uplift during the Quaternary and Neogene, *Earth Sci. Rev.*, *132*, 13–38, doi:10.1016/j.earscirev.2014.01.007.

Peltier, W. R. (1998), Postglacial variations in the level of the sea: Implications for climate dynamics and solid-Earth geophysics, *Rev. Geophys.*, *36*, 603–689, doi:10.1029/98RG02638.

Permanent Service for Mean Sea Level (PSMSL) (2013), *Tide Gauge Data*. Retrieved 02 Dec 2013 from http://www.psmsl.org/data/obtaining/.

Prandi, P., A. Cazenave, and M. Becker (2009), Is coastal mean sea level rising faster than the global mean? A comparison between tide gauges and satellite altimetry over 1993–2007, *Geophys. Res. Lett.*, *36*, L05602, doi:10.1029/2008GL036564.

Rahmstorf, S., G. Foster, and A. Cazenave (2012), Comparing climate projections to observations up to 2011, *Environ. Res. Lett.*, *7*(4), 044035, doi:10.1088/1748-9326/7/4/044035.

Ray, A., and K. Key (2012), Bayesian inversion of marine CSEM data with a trans-dimensional self parametrizing algorithm, *Geophys. J. Int.*, *191*, 1135–1151.

Ray, R. D., and B. C. Douglas (2011), Experiments in reconstructing twentieth-century sea levels, *Prog. Oceanogr.*, *91*, 496–515, doi:10.1016/j.pocean.2011.07.021.

Rhein, M., et al. (2013), Observations: Ocean, in *Climate Change 2013: The Physical Science Basis. Contribution of Working Group I to the Fifth Assessment Report of the Intergovernmental Panel on Climate Change*, edited by T. Stocker et al., pp. 385–428, Cambridge Univ. Press, Cambridge, U. K., and New York.

Royden, L. H., and D. J. Papanikolaou (2011), Slab segmentation and late Cenozoic disruption of the Hellenic arc, *Geochem. Geophys. Geosyst.*, *12*, Q03010, doi:10.1029/2010GC003280.

Sambridge, M., T. Bodin, K. Gallagher, and H. Tkalčić (2013), Transdimensional inference in the geosciences, *Philos. Trans. R. Soc. London, Ser. A*, *371*(1984), 20,110,547.

Serpelloni, E., C. Faccenna, G. Spada, D. Dong, and S. D. P. Williams (2013), Vertical GPS ground motion rates in the Euro-Mediterranean region: New evidence of velocity gradients at different spatial scales along the Nubia-Eurasia plate boundary, *J. Geophys. Res. Solid Earth*, *118*, 6003–6024, doi:10.1002/2013JB010102.

Sisson, S. (2005), Transdimensional Markov chains: A decade of progress and future perspectives, *J. Am. Stat. Assoc.*, *100*(471), 1077–1090.

Spada, G., and G. Galassi (2012), New estimates of secular sea level rise from tide gauge data and GIA modelling, *Geophys. J. Int.*, *191*, 1067–1094, doi:10.1111/j.1365-246X.2012.05663.x.

Stanev, E. V., and E. L. Peneva (2001), Regional sea level response to global climatic change: Black sea examples, *Global Planet. Change*, *32*(1), 33–47, doi:10.1016/S0921-8181(01)00148-5.

Syvitski, J. P. M., and A. Kettner (2011), Sediment flux and the Anthropocene, *Philos. Trans. R. Soc. London, Ser. A*, *369*, 957–975, doi:10.1098/rsta.2010.0329.

Tamisiea, M. E., J. X. Mitrovica, G. A. Milne, and J. L. Davis (2001), Global geoid and sea level changes due to present-day ice mass fluctuations, *J. Geophys. Res.*, *106*, 30,849–30,864, doi:10.1029/2000JB000011.

Tarantola, A., and B. Valette (1982), Inverse problems = quest for information, *J. Geophys.*, *50*(3), 150–170.

Tkalčić, H., M. Young, T. Bodin, S. Ngo, and M. Sambridge (2013), The shuffling rotation of the Earth/'s inner core revealed by earthquake doublets, *Nat. Geosci.*, *6*, 497–502.

Vassilakis, E., L. Royden, and D. Papanikolaou (2011), Kinematic links between subduction along the hellenic trench and extension in the Gulf of Corinth, Greece: A multidisciplinary analysis, *Earth Planet. Sci. Lett.*, *303*(12), 108–120, doi:10.1016/j.epsl.2010.12.054.

Voronoi, G. (1908), Nouvelles applications des parametres continus a la theorie des formes 1214 quadratiques, *J. Reine Angew. Math.*, *134*, 198–287.

Wenzel, M., and J. Schröter (2010), Reconstruction of regional mean sea level anomalies from tide gauges using neural networks, *J. Geophys. Res.*, *115*, C08013, doi:10.1029/2009JC005630.

White, N. J., J. A. Church, and J. M. Gregory (2005), Coastal and global averaged sea level rise for 1950 to 2000, *Geophys. Res. Lett.*, *32*, L01601, doi:10.1029/2004GL021391.

Woodworth, P. L. (1990), A search for accelerations in records of European mean sea level, *Int. J. Climatol.*, *10*, 129–143, doi:10.1002/joc.3370100203.

Woodworth, P. L., N. J. White, S. Jevrejeva, S. J. Holgate, J. A. Church, and W. R. Gehrels (2009), Evidence for the accelerations of sea level on multi-decade and century timescales, *Int. J. Climatol.*, *29*, 777–789, doi:10.1002/joc.1771.

Woodworth, P. L., M. Menśendez, and W. Roland Gehrels (2011), Evidence for century—Timescale acceleration in mean sea levels and for recent changes in extreme sea levels, *Surv. Geophys.*, *32*, 603–618, doi:10.1007/s10712-011-9112-8.

Wöppelmann, G., C. Letetrel, A. Santamaria, M.-N. Bouin, X. Collilieux, Z. Altamimi, S. D. P. Williams, and B. M. Miguez (2009), Rates of sea-level change over the past century in a geocentric reference frame, *Geophys. Res. Lett.*, *36*, L12607, doi:10.1029/2009GL038720.